國立臺灣大學電機資訊學院電子工程學研究所

碩士論文

Graduate Institute of Electronics Engineering

College of Electrical Engineering & Computer Science

National Taiwan University

Master Thesis

利用邊緣減薄結構提升量子點紅外光偵測器操作溫度之研究

Enhancement of Operation Temperature of Quantum Dot Infrared Photodetectors by Edge Thinning Structure

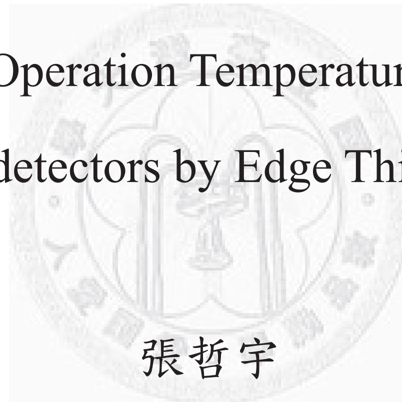

張哲宇

Chang Che-Yu

指導教授：李嗣涔 博士

Advisor: Lee Si-Chen, Ph.D.

中華民國一百年六月

June, 2011

國立臺灣大學碩士學位論文

口試委員會審定書

利用邊緣減薄結構提升量子點紅外光偵測器

操作溫度之研究

Enhancement of Operation Temperature of Quantum Dot Infrared Photodetectors by Edge Thinning Structure

本論文係張哲宇君（學號 R98943076）在國立臺灣大學電子工程學研究所，所完成之碩士學位論文，於民國一百年六月二十九日承下列考試委員審查通過及口試及格，特此證明

口試委員：

李嗣涔

（指導教授）

孫台平　　管傑雄

林浩雄

系主任、所長　張耀文

Content

誌謝 I

摘要 II

Abstract III

Chapter 1 Introduction 1

1.1 Introduction to Quantum Dot Infrared Photodetetors 1

1.2 Methods to Improve Operation Temperature 2

1.2.1 AlGaAs Blocking Layer 2

1.2.2 Surface Passivation 3

1.3 Edge Thinning Structure 3

1.4 Motivation and Outline 5

Chapter 2 The Fundamentals of Infrared Detectors and Experiments 6

2.1 Theory 6

2.1.1 Thermal Radiation 6

2.1.2 Infrared Detectors 7

2.1.3 Quantum Dot Infrared Photodetectors 10

2.2 Process Flow 13

2.2.1 Fabrication Processes 13

2.2.2 H_3PO_4-H_2O_2-H_2O Etching Solution 18

2.2.3 Lift-off Process 21

2.3 Measurement Systems 21

2.3.1 Current-Voltage Measurement 22

2.3.2 Introduction of FTIR 22

2.3.3 Relative Spectral Response 26

2.3.4 Absolute Responsivity 28

2.3.5 Specific Detectivity 31

2.4 Edge Thinning Introduction 32

2.5 Atomic Layer Deposition Mechanism and the transmission of Al_2O_3 in the infrared spectrum 34
Chapter 3 Edge Thinning Structure with Different Depths on QDIPs 38
3.1 The Effect of Edge Thinning Structure with Different Depths on IV Characteristics of QDIPs 39
3.1.1 Sample Preparation 39
3.1.2 Results and Discussion 41
3.2 The Effect of Edge Thinning Structure with Different Depths on photo-response of QDIPs 46
3.2.1 Sample Preparation 46
3.2.2 Results and Discussion 46
Chapter 4 The Combination of Edge Thinning Structure and Surface Passivation Layer on the Performance of QDIPs 50
4.1 Sample Preparation 51
4.2 Results and Discussion 54
Chapter 5 Conclusions 69
Bibliography 70

Figure Captions

Fig. 2.1 The Blackbody radiant existence under different temperatures. 8

Fig. 2.2 Schematic band diagrams of type Ⅰ and type Ⅱ heterojunction device.............. 9

Fig. 2.3 Density of states in bulk material (3D), quantum well (2D), quantum wire (1D), and quantum dot (0D). 11

Fig. 2.4 The flow chart of device fabrication and testing. 13

Fig. 2.5 Device fabrication processes of infrared photodetector, (a) the first photoresist coating, (b) the first developing, (c)the first wet etching, (d) photoresist cleaning, (e) the second photoresist coating, (f) the second developing, (g) the second wet etching, (h) photoresist cleaning, (i) the third photoresist coating (j) the third developing (k) metals evaporation , and (j) lift-off 14

Fig. 2.6 The etching rates of different composition ratios in H_3PO_4-H_2O_2-H_2O system..... 19

Fig. 2.7 The linear fitting of etching rate trials of $H_3PO_4/H_2O_2/H_2O$: 8ml/4ml/60ml etching solution. 20

Fig. 2.8 The uniformity at different etching depths. 20

Fig. 2.9 The I-V measurement system. 23

Fig. 2.10 The principle of Michelson interferometer. 24

Fig. 2.11 The setup to measure relative spectral response. 27

Fig. 2.12 The setup to measure absolute spectral response. 30

Fig. 2.13 The pinching off mechanism of edge thinning structure. 32

Fig. 2.14 The Al_2O_3 layer forming process sequence. 36

Fig. 2.15 The transmission of GaAs and GaAs with Al_2O_3 layer in the infrared spectrum. 37

Fig. 3.1 The schematic diagram of device structure (QDIP75). 40

Fig. 3.2 The schematic diagram of devices (a) A, the standard device without edge thinning structure, (b) B, the device with edge thinning structure at top contact layer, (c) C, the device with edge 40

Fig. 3.3 The I-V characteristic of device A. 42

Fig. 3.4 The I-V characteristic of device B. 43

Fig. 3.5 The I-V characteristic of device C. **44**

Fig. 3.6 The comparison of dark I-V characteristics of devices A, B , and C at T= (a) 20 K and (b) 90 K. **45**

Fig. 3.7 The responsivities of device A at T= (a) 20 K and (b) 120 K (the highest operation temperature) at different biases. **47**

Fig. 3.8 The responsivities of the device B at T= (a) 20 K and (b) 125 K (the highest operation temperature) at different biases. **48**

Fig. 3.9 The responsivities of device C at T= (a) 20 K and (b) 125 K (the highest operation temperature) at different biases. **49**

Fig. 4.1 The schematic structure of devices (a) D, the standard device with surface passivation by ALD Al_2O_3, (b) E, the device with edge thinning structure at top contact layer and surface passivation by ALD Al_2O_3, (c) F, the device with edge thinning structure at quantum dot layer and surface passivation by ALD Al_2O_3. .... **52**

Fig. 4.2 The fabrication processes of devices with edge thinning structure and surface passivation layer, (a) edge thinning structure formation (as Fig. 2.5 (a)-(h) show), (b) dip in HF / NH_4OH, (c) surface passivaiton layer Al_2O_3 by ALD, (d) RTA, (e) photoresist coating,

(f) developing, (g) wet etching Al_2O_3 by diluted HF, (h) metals evaporation, (i) lift off. **53**

Fig. 4.3 The I-V characteristic of device D. **56**

Fig. 4.4 The I-V characteristic of device E. **57**

Fig. 4.5 The I-V characteristic of device F. **58**

Fig. 4.6 The comparison of dark I-V characteristics of devices A and D at T= (a) 20 K and (b) 90 K. **59**

Fig. 4.7 The comparison of dark I-V characteristics of devices B and E at T= (a) 20 K and (b) 90 K. **60**

Fig. 4.8 The comparison of dark I-V characteristics of devices C and F at T= (a) 20 K and (b) 90 K. **61**

Fig. 4.9 The comparison of dark I-V characteristics of devices D, E, and F at T= (a) 20 K and (b) 90 K. **62**

Fig. 4.10 The comparison of photo I-V characteristics of devices (a) A and D, (b) B and E, and (c) C and F at T=20 K. **63**

Fig. 4.11 The responsivities of device D at T= (a) 20 K and (b) 130 K (the highest operation temperature) at different biases. 65

Fig. 4.12 The responsivities of device E at T= (a) 20 K and (b) 105 K (the highest operation temperature) at different biases. 66

Fig. 4.13 The responsivities of device F at T= (a) 20 K and (b) 135 K (the highest operation temperature) at different biases. 67

Fig. 4.14 The comparison of detectivities of devices A and F at bias voltage = (a) 0.6 volt and (b) 1.6 volt. 68

List of Tables

Table 2.1 Conditions and purposes of the cleaning solvent 17

Table 2.2 The photolithography conditions 17

Table 2.3 Evaporation condition... 17

誌謝

在台大兩年的研究所生活，將是我最珍貴的一段回憶。在這段日子，我學會實事求是、以誠待人；也建構起對未來的藍圖。

首先，必須向我的指導老師 李嗣涔 教授致上最深的感謝。除了給我研究上的指導，也教導我重視細節的處事「態度」，甚至與我分享對生命意義的價值觀，讓我更達觀的面對人生。黃珈擇與李政�兩位學長，給我的關心、幫助，是無法言喻的，但還是要說聲：「謝謝你們！你們就像我的大哥！」我會記得你們總是主動關心我量測結果如何、有沒有遇到問題；在我熬夜做實驗時，為我買杯飲料。祝福你們未來的博班生涯順利，並擁有璀璨的未來！

這段時間以來，許多人與我分享喜怒哀樂。尤其 249 室的每一位：善體人意的張議聰學長、成熟穩重的楊介宏學長、兒子很可愛的黃昭儒學長、幽默風趣的薛淳元學長、追女生好像很有一套的施怡仲學長、總是充滿鬥志，也帶給我很多啟發的余致緯、對科技產品不能自拔，偶爾陪我談心的李昶弘。和你們的回憶有討論實驗的認真、一起玩樂的歡笑、互相消遣的幽默風趣。此外，陳鴻欣學長、莊芳慈學長、黃紹宇也給我許多的幫助；助理馬姐總耐心盡責地幫我們處理許多事務，就像大家的保姆一樣。謝謝你們陪我走過碩班生涯，祝你們未來一切順心！也為學弟們：陳俊翰、顏永恩、陳又誠、邱大晟、林雨德、紀承諭加油！祝你們研究順利！

研究之外的活動，讓我更瞭解自己、更清楚未來的方向。我要感謝曾經和我一起並肩作戰的每一位夥伴：創業課的 Simphony，你們陪我一起寫出我人生中的第一份 business plan，讓我對企業營運有基礎的認識。YEF 的 NINO，你們讓我學會如何傾聽隊友、在困境中咬緊牙關撐到最後；Entrepreneurial Marketing Group，你們給了我一個改進自己的機會，讓我體會到自己真的進步了；Hallowin，你們讓我學會如何當一個學長，穩定團隊的信心、鼓舞團隊的士氣。尤其要特別感謝我的拍檔，俊佑。能認識你是我這兩年最珍貴的收穫之一！還有一起玩音樂的夥伴：總是幫我做球，讓我有機會認識正妹的張健峰老師、和我同樣熱愛節奏藍調，合作無間的 Etzer Emile。此外，要特別感謝幾位給我支持、鼓勵的前輩：清大的游萃蓉老師、YEF 的李滿營業師、李聖珉業師。你們是我的典範，讓我能堅守待人處事的原則、並勇於抉擇未來的方向。

最重要的，要感謝我的家人。你們給了我一個避風港，無論受到任何挫折，我都還能回到溫暖的家。特別感謝我的母親 朱美榮 女士，總是給我無微不至的關愛、支持，謝謝您。

感謝上帝，給我這美好的兩年，在台大遇見豐富的人、事、物，讓我學習、成長許多。這段時光會珍藏在我心中，並轉化為邁向未來的原動力。

摘要

本文的研究目標是提升量子點紅外光偵測器的操作溫度。主要嘗試利用邊緣減薄結構;結合表面原子層沉積氧化鋁層的邊緣減薄結構,減低元件表面漏電流,提高操作溫度。

本文在第一個實驗中,研究了在上電極層、量子點層,兩個不同位置的邊緣減薄結構對元件性能的影響。所採用的邊緣減薄結構厚度約為100~200 nm,寬度約為10 μm。實驗結果發現,邊緣減薄結構並無法有效降低量子點紅外光偵測器的暗電流並提升操作溫度。

本文在第二個實驗中,結合了邊緣減薄結構與表面原子層沉積的氧化鋁層,嘗試提升元件的操作溫度。所沉積的氧化鋁約為10 nm厚。實驗結果發現,結合邊緣減薄結構與表面原子層沉積氧化鋁層仍無法顯著提升量子點紅外光偵測器的操作溫度。但位於量子點層的邊緣減薄結構與表面原子層沉積氧化鋁層結合後,能夠抑制元件的電流,使元件能在更高的電壓下工作。

在本文的實驗中,無法藉由邊緣減薄結構,以及與表面原子層沉積氧化鋁層結合的邊緣減薄結構顯著提升量子點紅外光偵測器的操作溫度。相關研究仍有待進一步的探討。

Abstract

In this thesis, the edge thinning structure with width of 10 μm and thickness of 100~200 nm and the edge thinning structure combined with surface passivation layer Al_2O_3 with thickness of 10 nm are adopted on n-i-n InAs/GaAs QDIPs to enhance the operation temperature of n-i-n InAs/GaAs quantum dot infrared photodetectors.

In the first experiment, edge thinning structure with different depths on QDIPs is investigated. It is found that edge thinning structure at top contact layer and quantum dot layer both can't significantly reduce the dark current and enhance the operation temperature of QDIPs in this experiment.

In the second experiment, the combination of edge thinning structure and surface passivation layer Al_2O_3 is investigated. It is found that the combination of edge thinning structure and surface passivation layer Al_2O_3 can't significantly reduce the dark current and enhance the operation temperature of QDIPs in this experiment. However, the combination of edge thinning structure at quantum dot layer and surface passivation layer Al_2O_3 can reduce the current by 2 orders of magnitude so the device can work at higher bias voltage.

In summary, the edge thinning structure and that combined with surface passivation layer Al_2O_3 haven't enhanced the operation temperature of QDIPs. It may require more advanced investigation.

Chapter 1 Introduction

1.1 Introduction to Quantum Dot Infrared Photodetetors

At room temperature, objects emit most of their energy in the form of infrared radiation. (with wavelength ranging from ~1 to 100μm) Since infrared photodetector is able to transfer the infrared radiation into electrical signal, it has been applied to varieties of field such as night vision camera, military recognition system, chemical spectroscopy and remote sensing [1-2].

In past few years, many works have investigated on the fabrication of the infrared photodetector based on low dimensional quantum structure including quantum dot (QD), quantum well (QW) and dot in the well structure [3-6]. Compared with quantum well infrared photodetectors (QWIPs), quantum dot infrared photodetectors (QDIPs) have some advantages: first, QDIPs are sensitive to normal-incident radiation by breaking of the polarization selection rule [7]. Second, QDIPs have the potential of high-temperature operation. (>100 K) It's because of the QDIPs low dark current resulting from the three-dimensional confinement of the electrons in quantum dots [8]. Although it has been investigated that QD structure has higher operation temperature and higher normal incident absorption than QW structure does, it still requires efforts to reach room-temperature operation.

1.2 Methods to Improve Operation Temperature

With increasing temperature, the dark current increases and eventually prevails the signal from photodetectors. This phenomenon limits the operation temperature of QDIPs. On the other hand, high cost of cooling systems makes QDIPs hard to be put into practical application [9]. Therefore, elevating the operation temperature has become the focus of research about QDIPs. To achieve high operation temperature, the dark current of the device has to be reduced. The dark current consists of two components, which are the dark current in the bulk and the surface leakage current at the surface. There are two methods to improve operation temperature of QDIPs as described below.

1.2.1 AlGaAs Blocking Layer

Wang *et al*. [10] discovered that an AlGaAs current blocking layer with high band gap can effectively reduce the dark current in the bulk and enhance the detectivity of QDIPs. In advance, Tang *et al*. [11] adopted double AlGaAs blocking layer on QDIPs and raised the operation temperature up to near room temperature (250 K).

1.2.2 Surface Passivation

Lai *et al*. [12], adopted surface passivation by atomic layer deposition to enhance the operation temperature. The Al_2O_3 surface passivation layer can fix the surface defect such as dangling bond generated by the wet etching process and reduce the surface leakage. Therefore the operation temperature can be enhanced by about 40 K.

1.3 Edge Thinning Structure

Lin and Lee [13], Wu *et al*. [14] adopted the emitter edge-thinning structure on AlGaAs/GaAs single heterojunction bipolar transistors and double-heterostructure-emitter bipolar transistor to improve the current gain. The emitter edge was etched down so that the surface and emitter-base junction depletion regions could overlap and pinch off the conducting channel near the surface, hence the current is blocked from the emitter periphery and the surface leakage current is reduced which enhances the current gain.

Fu *et al*. [15] observed a strong downward-band-bending phenomenon at the edge of emitter-edge-thinning intersection with the exposed base surface. The band bending induced a potential saddle point, which increased the recombination rates and electron densities. The emitter-edge-thinning thickness is critical in reducing surface recombination at the potential saddle point.

From simulation results, if the thickness of the emitter-edge-thinning structure is too thick, an additional leakage path will be developed which results in the increase of electron densities and recombination rates at the edge of the emitter-edge-thinning structure. On the contrast, if the thickness of the emitter-edge-thinning structure is too thin, the blocking effect on electrons will deteriorate seriously.

The experimental results match the simulation results well. And the optimum thickness of the emitter-edge-thinning structure is reckoned between 10 and 20 nm.

1.4 Motivation and Outline

In order to elevate the QDIPs' operation temperature, the combination of edge thinning and passivation layer is adopted in this work to reduce surface leakage current and consequently increase the operation temperature.

In chapter 2, the basic concepts of infrared detection and the fundamental theory of the quantum dot infrared photodetectors (QDIPs) will be introduced. The measurement system and fabrication process will be specified. The experimental methods to measure the relative spectral response and to calculate the absolute responsivity of QDIPs will be described. The mechanism of edge thinning will also be described in detail.

In chapter 3, the effect of edge thinning structure on quantum dot infrared QDIPs and the effect of different depth of edge thinning structure will be investigated.

In chapter 4, the effect of combination of edge thinning structure and surface passivation layer Al_2O_3 by atomic layer deposition and edge thinning structure will be investigated.

Finally, the conclusion is given in chapter 5.

Chapter 2 The Fundamentals of Infrared Detectors and Experiments

In this chapter, the basic concepts of infrared detector will be introduced. Various infrared photodetectors and their characteristics will be described. The fundamental theory of the quantum-dot infrared photodetector (QDIP) will be given here and the fabrication processes of the QDIP will be described in this chapter also.

2.1 Theory

2.1.1 Thermal Radiation

Thermal radiation is the electromagnetic wave emitted from thermal objects. In nature, all objects emit thermal radiation at temperature above absolute zero. Infrared detector can be applied to detect the thermal signals carrying some information of the thermal object.

The thermal radiation emitted from a perfect blackbody follows the Planck law [9].

$$M_{e,\lambda}(\lambda,T) = \frac{2\pi hc^2}{\lambda^5[e^{hc/\lambda kT}-1]} = \frac{3.74\times10^4}{\lambda^5[e^{14388/\lambda T}-1]} \qquad (2\text{-}1)$$

where $M_{e,\lambda}(\lambda,T)$ is the spectral radiant intensity in watts per square centimeter of area and micrometer of radiation wavelength ($\mathrm{Wcm^{-2}\mu m^{-1}}$), λ , the emitted

wavelength in micrometers (μm), *T,* is the absolute temperature of the blackbody in Kelvins (K), *h,* the Plank's constant (6.626×10^{-34} $Wsec^2$), *c,* the speed of light (3×10^{10} cm sec^{-1}), *k,* the Boltzmann's constant (1.38×10^{-23} W sec K^{-1}).

Figure 2.1 shows the blackbody radiation spectra at different temperature from 250 to 450 K, the infrared energy shifts to shorter wavelengths at room temperature and the infrared radiation wavelength at higher temperature is in the range of 3 to 25 μm. For thermal imaging, there are two atmospheric windows of interest. One is located at 3 to 5 μm band, the other is at 8 to 12 μm band [10].

2.1.2 Infrared Detectors

Infrared detectors are usually categorized as either thermal or photon devices. The absorption of light in thermal detectors raises the temperature of the devices, which in turn changes some temperature-dependent parameters such as electrical conductivity. The absorption of infrared radiation in photon (quantum) detectors results directly in some specific quantum events such as photoelectric emission from a surface or electronic interband transitions in semiconductor materials [11].

For long wavelength IR detection (8 to 12 μm), it can be divided into type I and type Ⅱ heterojunction devices. Fig. 2.2(a) and (b) show the band diagrams and electron transfer properties of these two type of device respectively. Furthermore, intrinsic and extrinsic or quantum well infrared detectors can be applied [12] to very

long wavelength IR detection (>12 μm),

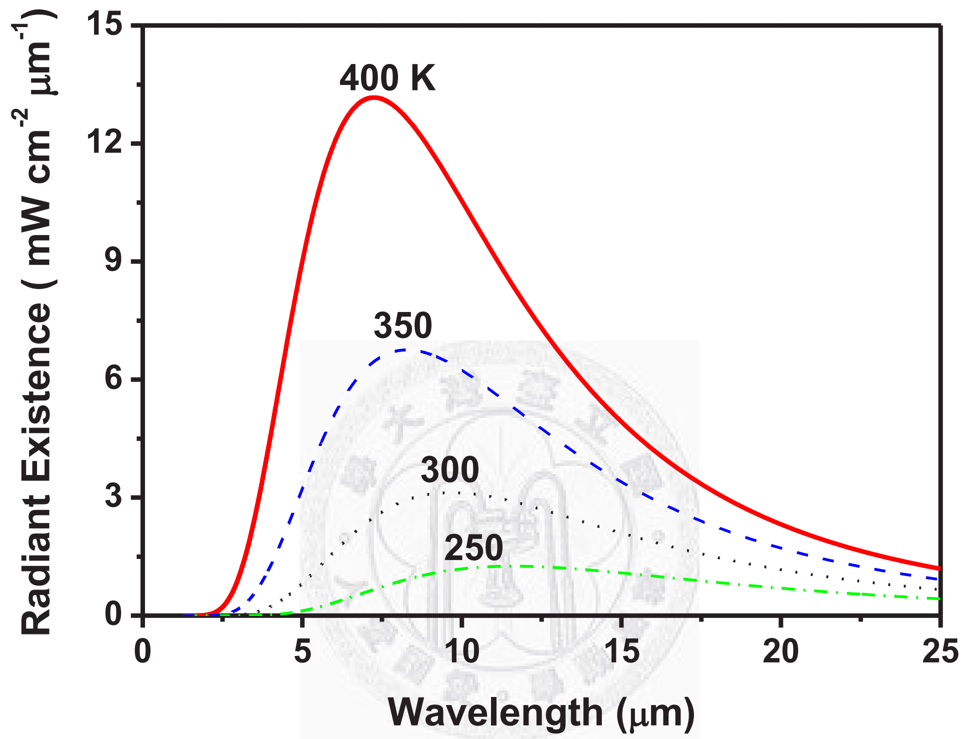

Fig. 2.1 The Blackbody radiant existence under different temperatures.

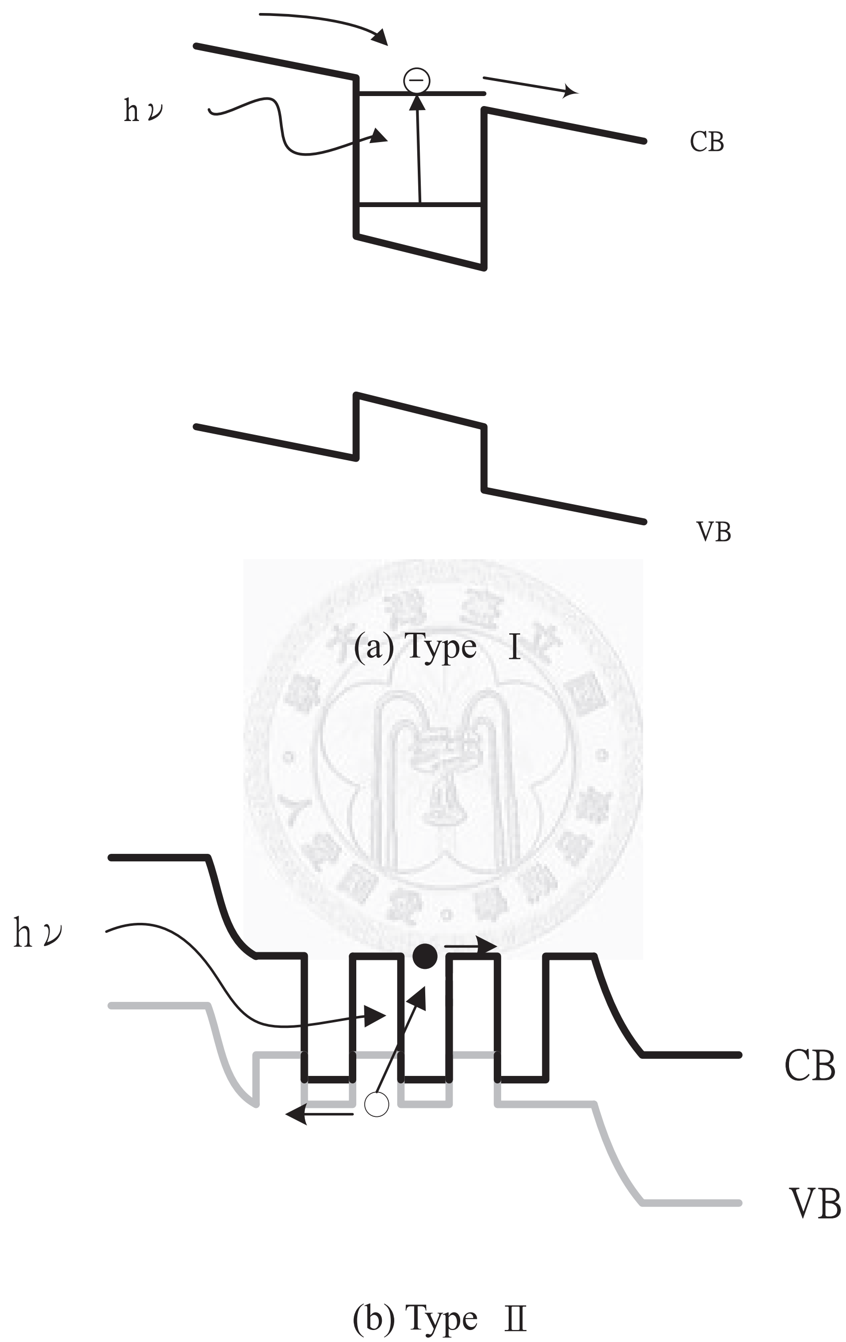

Fig. 2.2 Schematic band diagrams of type Ⅰ and type Ⅱ heterojunction device.

Quantum infrared photodetector, such as superlattice infrared photodetector (SLIP), quantum well infrared photodetector (QWIP) and quantum dot infrared photodetector (QDIP) have attracted considerable interest during recent years [13-15]. These structures are made of semiconductor materials by the presence of intersubband transition for their operation. Unlike the detection by interband transition, which limited to the intrinsic bandgap energy of the material, the detection by intersubband transition can vary the absorption energy by changing the structure of the detector.

QWIP and SLIP can be easily fabricated by epitaxial growth, which have regular periodic arrangement. Because of selection rule in QWIP, light-coupling structure must be used. Over past few years, QDIPs have been widely investigated in infrared detection[16-19]. In principle, these nanostructures provide a three dimensional (3D) confinement potential for the carriers and consequently have a discrete energy spectrum with δ -like densities of states (DOS). Fig. 2.3 shows the density of states of materials with different dimensions. Because of non-uniformity and strain effect in QDs [20-22], there exist many unresolved issues worthy of investigation.

2.1.3 Quantum Dot Infrared Photodetectors

Quantum-dots (QDs) provide the ultimate quantum system with a three-dimension carrier confinement resulting in discrete electronic energy state.

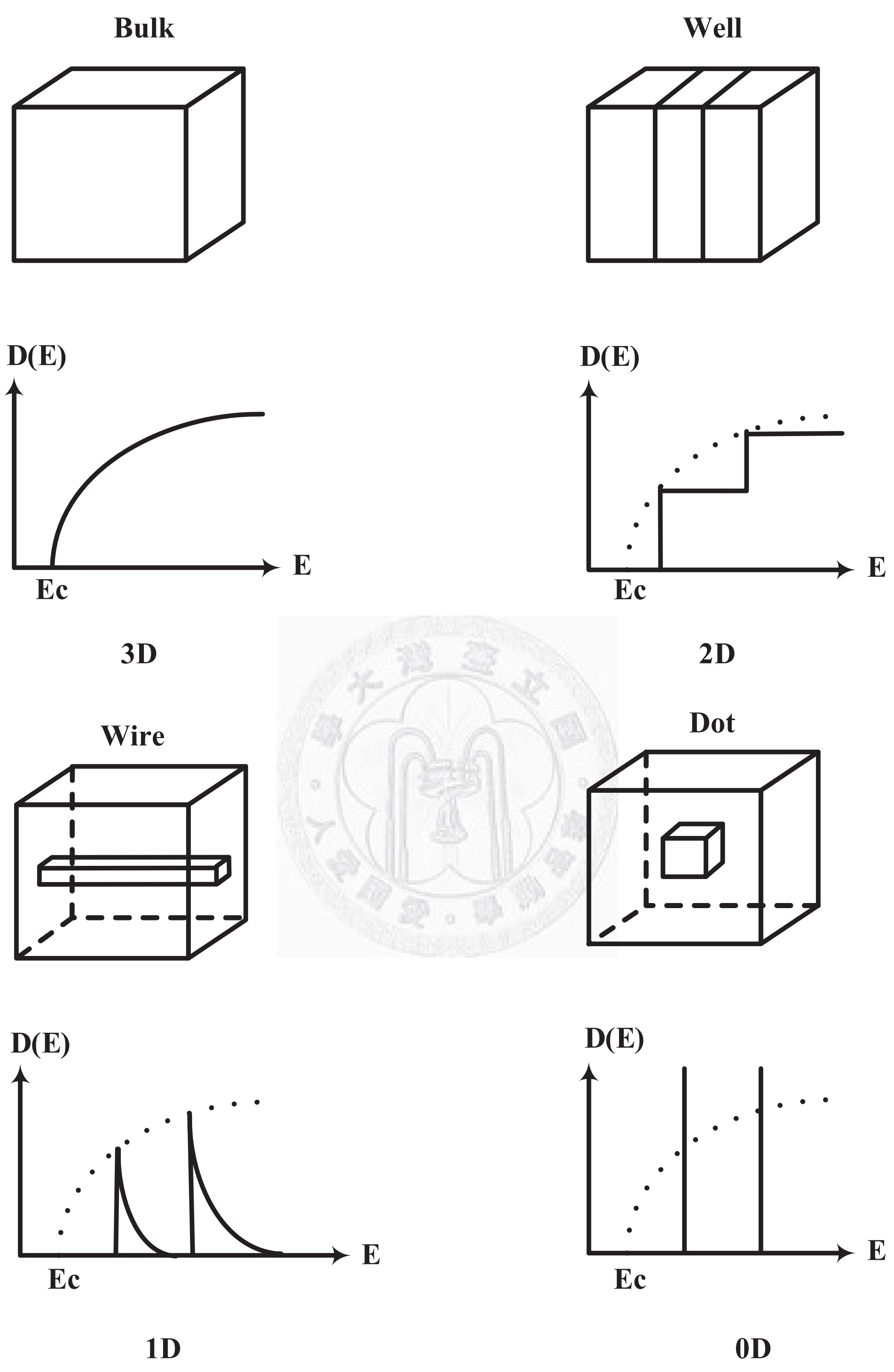

Fig. 2.3 Density of states in bulk material (3D), quantum well (2D), quantum wire (1D), and quantum dot (0D).

Great effort has been made for fabricating quantum dot structure by means of etching or local diffusion of quantum wells [23], selective growth [24-25], self-organized growth [26].

Self-organized growth of quantum dots has been demonstrated using both molecular beam epitaxy (MBE) and metal-organic chemical vapor deposition (MOCVD)[27]. The growth methods offer the distinct advantage of producing defect-free QD structures. From the Stranski-Ḱrastanov (SK) growth mode, the mismatch between substrate and wetting layer and the resulting strain have been considered to be responsible for the driving force for the formation of QDs.

QDIP is one of the applications of QD heterostructures. Compared to QWIP and SLIP, QDIP's advantages are high responsivity, low dark current,. polarization independent, broad-band detection spectrum and high temperature operation. Due to non-uniformity of QDs, the broad-band spectrum can be observed. Furtherrmore, zero dimensional QDs results in δ-like densities of states and 3D confinement of electrons on space geometry cause the possibility of room temperature operation.

Direct imaging methods, such as scanning tunneling microscopy (STM), atomic force microscopy (AFM), and transmission electron microscopy (TEM) can be used to study the surface morphology of QDs. Photoluminescence (PL) have been used to describe optical properties of InAs/GaAs QDs [28].

2.2 Process Flow

A flow chart of the device fabrication and testing is shown in Fig. 2.4, and the details will be described latter.

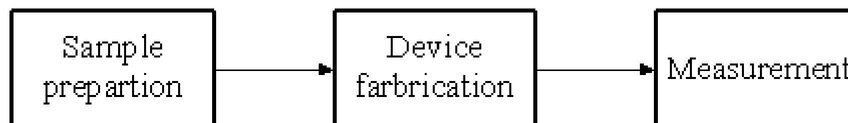

Fig. 2.4 The flow chart of device fabrication and testing.

2.2.1 Fabrication Processes

For better device performance, any defects caused in the process sequence should be minimized. Etching depth, ohmic contact and optical coupling into the devices are important issues that require much attention.

This section will describe the device fabrication processes in details. Fig.2.5 shows the fabrication process sequences of quantum dot infrared photodetectors.

(1) Surface cleaning

Cleaning refers to removing undesired materials from the wafer before subsequent process steps. Cleaning operations are performed before all major steps during device processing for better reliability and performance. These steps

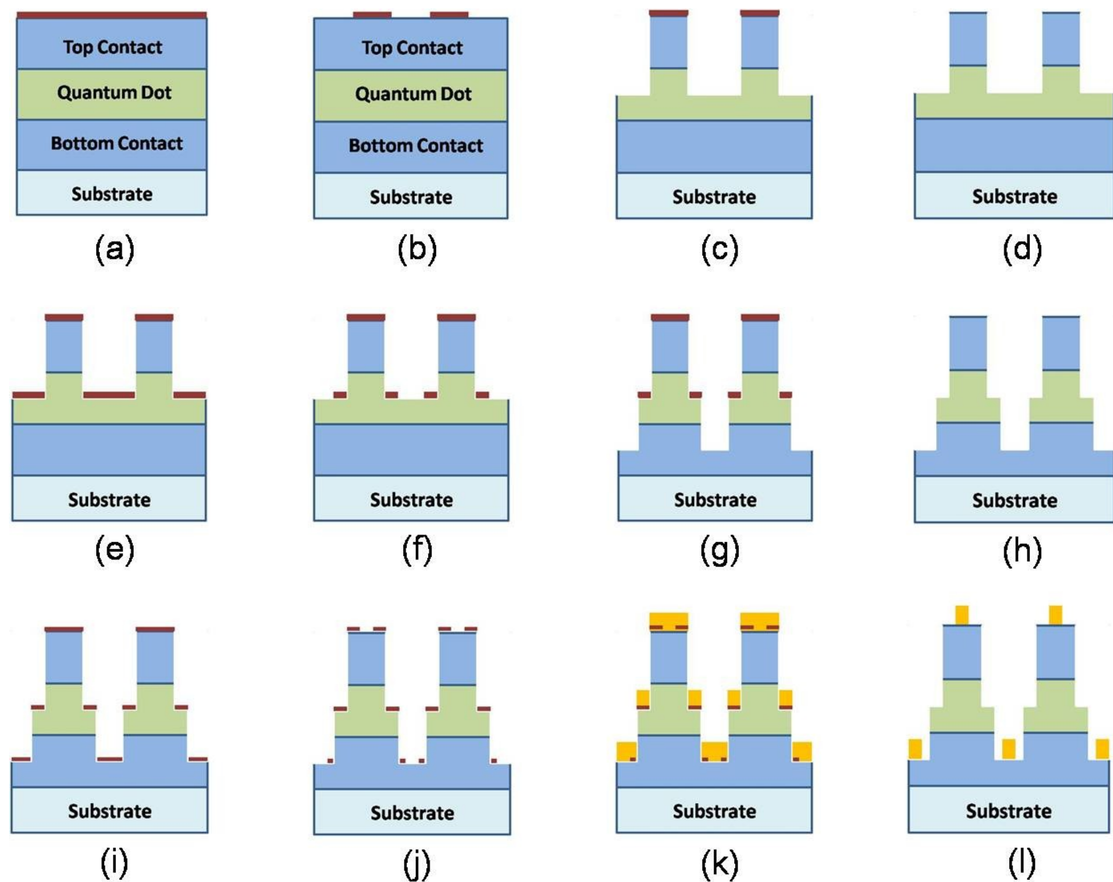

Fig. 2.5 Device fabrication processes of infrared photodetector, (a) the first photoresist coating, (b) the first developing, (c)the first wet etching, (d) photoresist cleaning, (e) the second photoresist coating, (f) the second developing, (g) the second wet etching, (h) photoresist cleaning, (i) the third photoresist coating (j) the third developing (k) metals evaporation , and (j) lift-off.

may employ organic solvents, vapor degreasing, and acids. We use organic solvents to remove oils, greases, particles and organic material such as photoresist and to keep the surface clean. Table 2.1 lists the cleaning conditions and purposes of the solvent.

(2) Formation of mesa structure

The process of mesa structure formation includes two stages, which are lithography and etching.

In lithography stage, SHIPLEY S1813 positive photoresist was spun and coated on the sample surface first and soft baked it 5 minutes to evaporate solvent contained in the photoresist. Soft baking before exposure is necessary because photoresist freshly spun is sticky. SHIPLEY MF-319 development solution was used to remove the portion of photoresist exposed. Finally, 20 minutes hard baking was used to formalize the pattern. The conditions of photo-lithography are listed in Table 2.2.

In etching stage, wet etching by liquid chemical etchant is adopted to remove the portion of epilayers without protection of photoresist. Such an etching procedure is an important part of various processing steps.

For device without edge thinning as control group, the epilayer is etched down to contact layer. For device with edge thinning as experimental group, it's etched down to the designated depth. The etching depth is measured by a surface profile. The etching solution will be discussed in section 2.2.3. After wet etching, $280\times180\ \mu m^2$

mesa structure was formed for device isolation.

(3) Formation of edge thinning structure

After mesa structure has been formed, device with edge thinning structure requires a similar lithography process to form a larger pattern ($300\times200\ \mu m^2$) which includes the width of edge . Then it's etched down to the contact layer to reduce the thickness of edge and the edge thinning structure is formed

(4) Formation of contact

The third photolithography mask was used to define the region of contact. Finally, Au/Ge/Ni alloy and Au were evaporated under the pressure of 6×10^{-6} torr. Table 2.3 lists the alloy type, thickness, and deposition rate. The sample was put in the rapid thermal annealer (RTA) to anneal for ohmic contact formation. The anneal rate is 420 ^{o}C/min up to the temperature of 420 ^{o}C for 120 seconds.

Table 2.1 Conditions and purposes of the cleaning solvent

Chemical Solution	Clean Time (min)	purposes
Acetone (CH_3COCH_3)	5	Clean photoresist, organism
Methanol (CH_3OH)	5	Clean Acetone
D.I water (H_2O)	5	Clean Methanol

Table 2.2 The photolithography conditions

Pattern Formation	Conditions
Spinning and Coating	4000 rpm 40 sec
Soft bake	90 ^{o}C 5 min
Exposure	15 sec
Development	20 sec
Hard bake	90 ^{o}C 20 min

Table 2.3 Evaporation condition

Source	Thickness (nm)	Evaporation rate (nm/sec)
Au/Ge/Ni (84 / 12 / 4)	70	0.05 ~ 0.1
Au	230	0.1 ~ 0.2

2.2.2 H_3PO_4-H_2O_2-H_2O Etching Solution

Wet etching proceeds through chemical reactions at the surface of the material. For chemical reactions to take place, the etchant species must reach the surface and react with the material appropriately. The reaction products must be removed from the surface. Almost all GaAs etchants operate by first oxidizing the surface and then dissolving the oxide, thereby removing some of the Gallium and Arsenic atoms. Generally, the etchant contains one component that acts as the oxidizer and the other that acts as the dissolving agent [29]. The H_2O_2 is the oxidizing agent and H_3PO_4 is the dissolving agent. For better control over the etching depth, the etching solution is 85% H_3PO_4 : H_2O_2 : H_2O = 2 : 1 : 15 (8ml: 4ml: 60ml). Fig. 2.7 displays the linear fitting of etching rate trials with different etching time. The etching rate can be reckoned as about 7 nm/sec and the deviation is about 0.5 nm/sec. Fig. 2.8 displays the etching uniformity at different etching depths. The uniformity can be reckoned as about 40 nm. Although it etches GaAs to some degree in almost all compositions, GaAs will not be etched in either H_2O_2 or H_3PO_4 alone.

Freshly mixed etchants may be hot, because exothermic reaction occurs when H_3PO_4 mixed with H_2O. As all chemical reactions, etching rate is sensitive to the temperature. So the etchant should be cooled to a steady temperature at least for 30 min after mixing. From our experiment, the etching rate for GaAs is about 6~8

nm/sec at 20 °C.

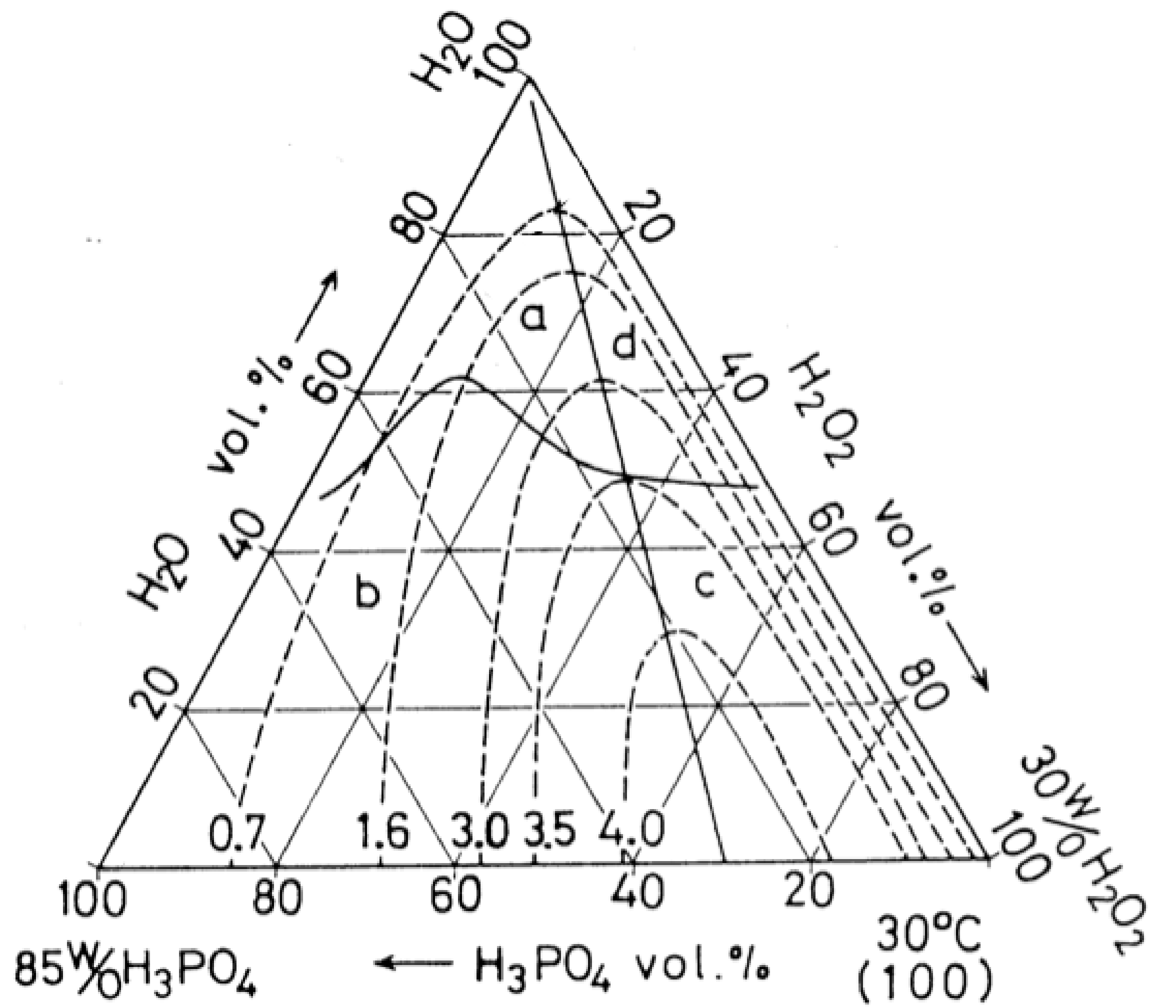

Fig. 2.6 The etching rates of different composition ratios in

H_3PO_4-H_2O_2-H_2O system.

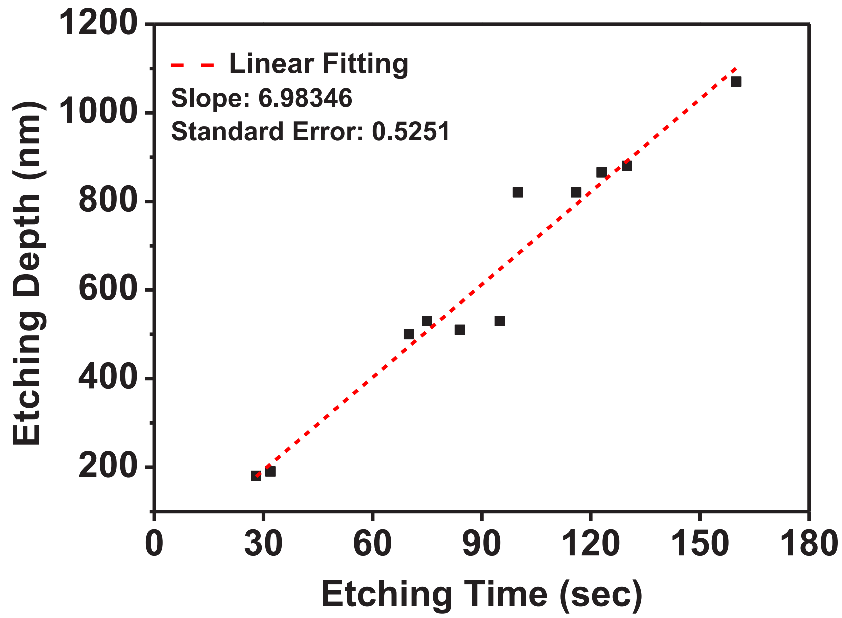

Fig. 2.7 The linear fitting of etching rate trials of $H_3PO_4/H_2O_2/H_2O$: 8ml/4ml/60ml etching solution.

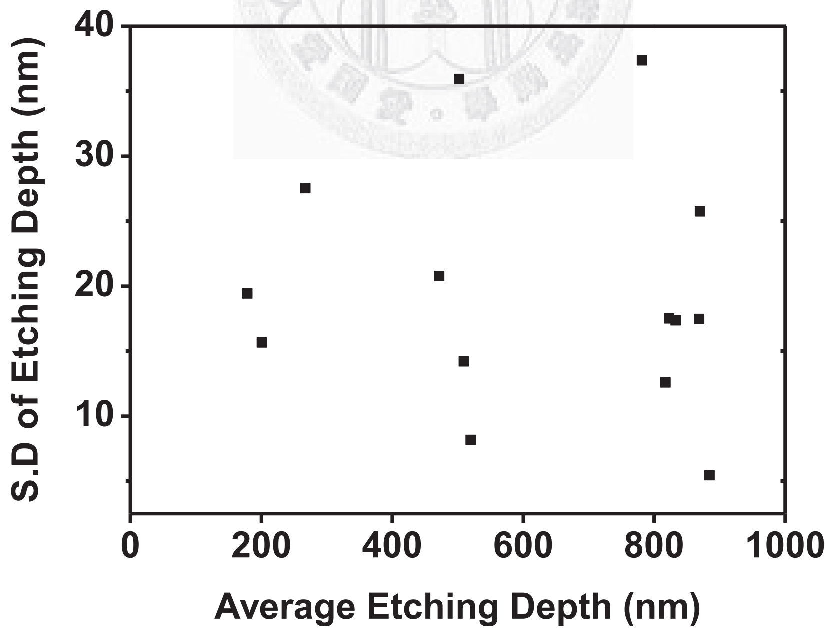

Fig. 2.8 The uniformity at different etching depths.

2.2.3 Lift-off Process

Lift-off is a very important procedure in the process flow. Device fabrication may work in vain, if lift-off process fails. Two important issues should be noticed, which can make lift-off process success and reduce the process time. (a) Photoresist should be thicker and hard-baking is not needed at the third photolithography step. (b) The sample could be adhered on a piece of glass before metalization. The sample holder of the evaporation system is made of metal. When the gold or alloy evaporated to the sample, it also evaporated to the sample holder. The holder was heated and transferred heat to the sample. The photoresist would be heated to become harder which was difficult to dissolve afterwards by acetone. The glass can retard the heat transfer from the holder. Following these two procedures make the lift-off process easier.

2.3 Measurement Systems

After devices are made, the performance of the device is tested, such as current-voltage measurement at various temperatures, the relative spectral response, responsivity and the calculation of the specific detectivity (D*). The various measurement systems will be described later.

2.3.1 Current-Voltage Measurement

The devices were bonded on the ceramic plates. The devices with larger resistance at 77 K are chosen to be measured. All the current-voltage (I-V) measurements were done by the HP4145B semiconductor parameter analyzer at various temperatures (10 ~ 200 K) in the cryogenic system. The dark current measurements were measured by carefully shielding the device from the background infrared radiation. For photocurrent measurement, the radiation shield is taken off. The system for the current-voltage measurement is shown in Fig. 2.9.

2.3.2 Introduction of FTIR

The infrared spectroscopy is an efficient method to reveal the properties of electrons in the minibands of superlattices and the performance of infrared photodetectors. Unlike the traditional infrared spectrometers which use the grating to detect each frequency component's absorption to get the whole spectral response, the Fourier Transform Infrared (FTIR) spectrometer uses the Michelson interferometer to get the whole spectral response simultaneously. We choose the FTIR spectrometer to measure our detector's quality. So the detail knowledge of FTIR is necessary.

At the heart of an FTIR spectrometer is a Michelson interferometer, as shown in Fig. 2.10. It consists of three active components: a moving mirror, a fixed mirror, and

a beamsplitter. The radiation from the broad-band IR source impinges on the

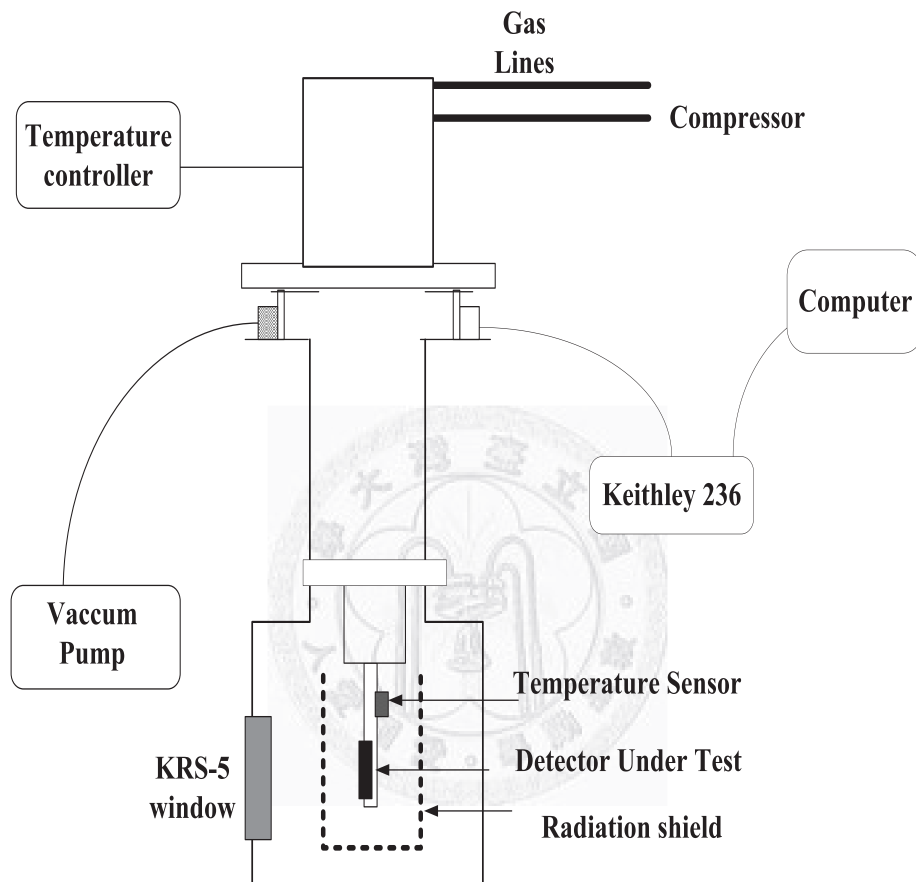

Fig. 2.9 The I-V measurement system.

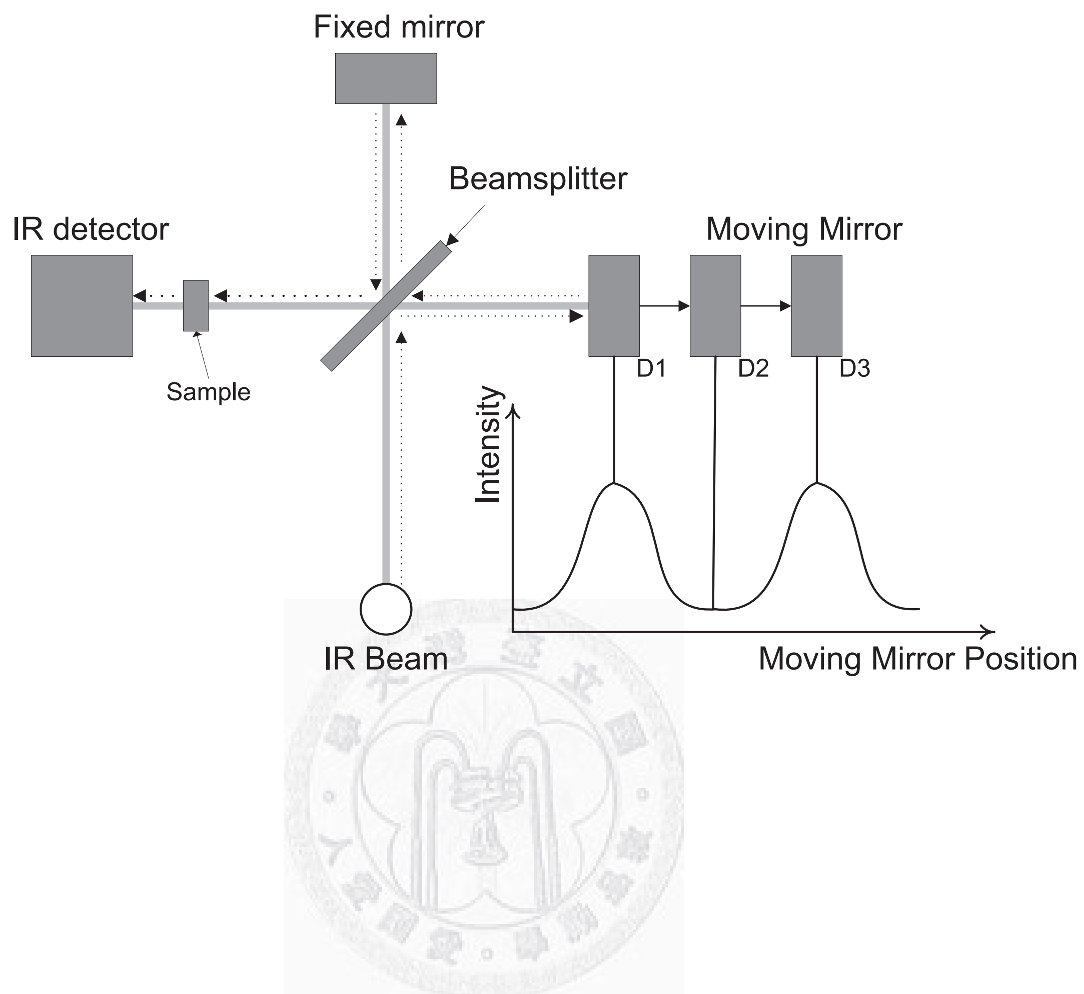

Fig. 2.10 The principle of Michelson interferometer.

beamsplitter, half the IR beam transmits to the fixed mirror and the remaining half reflects to the moving mirror. Then, those divided beams reflect back to the beamsplitter and recombine to generate the interference pattern. The resulting beam passes through the sample and finally impinges upon the detector. We first consider a frequency f' component of IR source. The intensity of the interfered beam depends on the optical pass difference between two split beams. The inset in Fig. 2.8 is the "interferogram", which is the record of the interference signal. When the moving mirror is moved with a constant velocity, the intensity of radiation reaching the detector is a sinusoidal manner. The intensity of the sinusoidal wave will reduce if the sample absorbs in this frequency f'. Then, the FTIR spectrometer takes the summation of superimposed sinusoidal waves, each wave corresponding to a signal frequency, to get the whole interference patterns [30].

The interferogram is a time domain spectrum. By using the Fourier transformation, we can convert the interferogram into a frequency domain spectrum to show the intensity as a function of frequency.

2.3.3 Relative Spectral Response

Spectral response measurement is used to measure relative output electrical signal as a function of wavelengths of incident infrared radiation. The entire system for measuring the spectral response is shown in Fig. 2.11.

Our system adopted PERKIN ELMER Fourier Transform Infrared Spectrometer (FTIR). The FTIR spectrometer has several basic advantages over a classical dispersive instrument, such as simultaneous measurement of the source wavelength, higher energy throughput, negligible stray light, constant resolution and no discontinuities. The detector was plastered on the closed-cycle cryostat system by the copper adhesive tape. The infrared radiation is incident on the detector by passing through the KRS-5 window to filter out the visible light and incident on the detector to excite photo-electrons. The current was transferred into voltage signal by STANFORD RESEARCH SYSTEM model SR570 transconductance preamplifier and then the preamplified signal is converted into spectral by Fourier Transform. Since the measured spectrums include background spectral response, we recorded this background by the pyroelectric detector of FTIR first and then ratio the measured spectrums against it to get the relative spectral response.

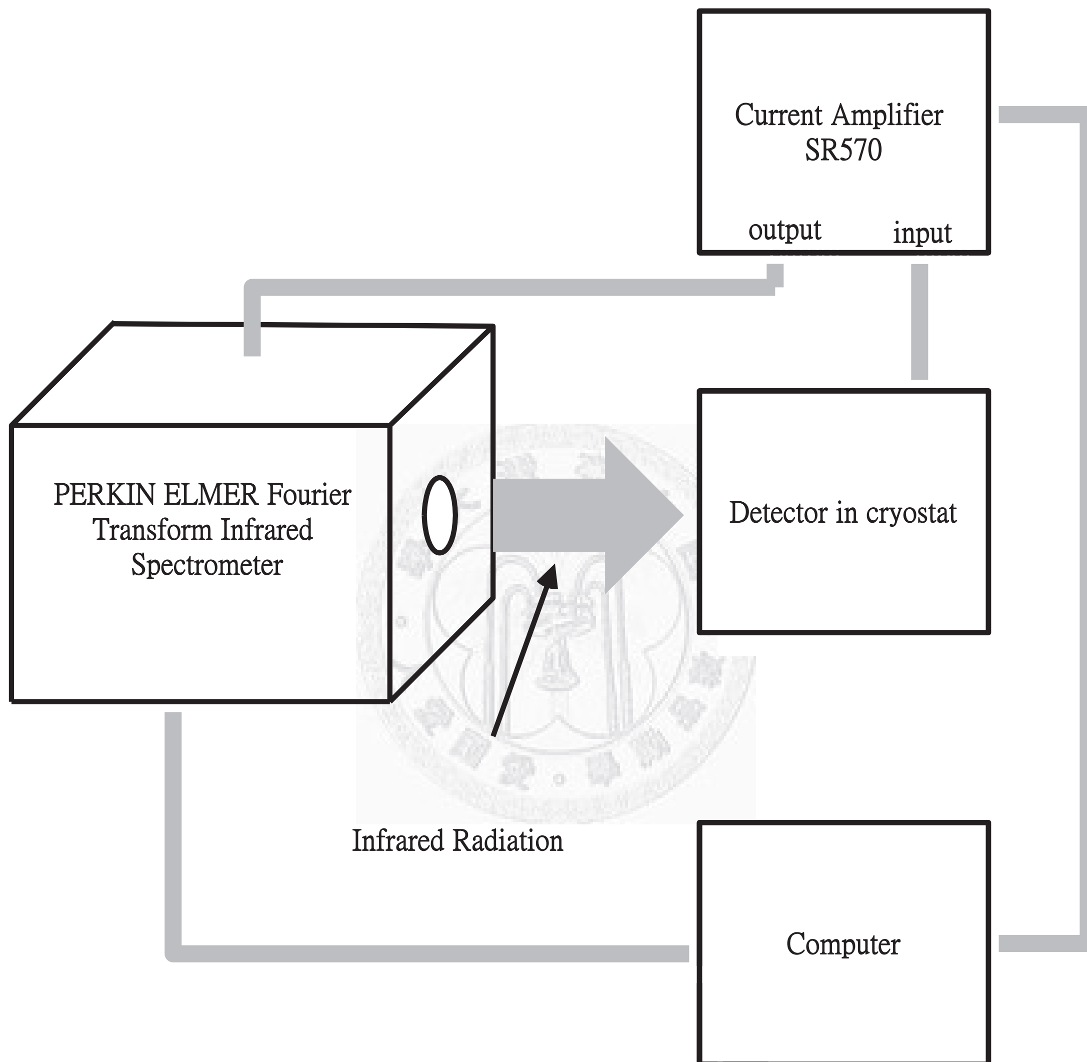

Fig. 2.11 The setup to measure relative spectral response.

2.3.4 Absolute Responsivity

After the relative response is taken, the blackbody radiation at high temperature is used to get the absolute responsivity. Responsivity is the ratio of the output S (usually in amperes or volts) to the radiant input $\phi e(\lambda)$ (in watts). Considered blackbody source at temperature T modulated at a frequency f that produces the observed output

$$R(T,f) = \frac{S}{\int \phi e(\lambda) d\lambda} \qquad (2\text{-}1)$$

Where λ is the wavelength of radiation, S is the output signal, $\phi e(\lambda)$ is the input radiation power. T and f express blackbody source temperature and chopper frequency.

Figure 2.12 displays the schematic diagram showing the setup for measuring the responsivity. The blackbody source is 800 K for a thermal infrared detector test. The variable-speed chopper modulates the signal at a frequency f by rotating a notched wheel in front of the source. The notches alternately cover and uncover the source, producing a nearly square-wave signal if the source aperture is small compared to the notch width. The detector is located at a known distance from the source so that the signal on the detector can be calculated. The photocurrent with applied bias was amplified by SR570 current preamplifier and transferred into the voltage signal. Both

the chopper frequency controller and the preamplifier signal were connected with SR830 DSP lock-in-amplifier to demodulate the voltage signal.

The absolute peak responsivity (R_{peak}) formula can be obtained by measuring both the responsivity and the relative spectral response

$$R_{peak} = \frac{S}{A_{BB} A_d T_{KRS-5} T_{GaAs} F_F / R^2 \times [\frac{\int_0^\infty R'(\lambda) M(\lambda, T_{BB}) d\lambda}{\pi} - \frac{\int_0^\infty R'(\lambda) M(\lambda, T_{rm}) d\lambda}{\pi}]} \quad (2\text{-}2)$$

Where S is the photo-voltage measured by lock-in-amplifier, A_{BB}, A_d are areas of blackbody source and detector, respectively, T_{KRS-5}, T_{GaAs} are transmission coefficients of *KRS-5 windows* (0.7) and GaAs (0.8) respectively, F_F is chopper modulation factor and our system is 0.45, R is the distance between blackbody source and detector, T_{BB}, T_{rm} are absolute temperature of blackbody source (800 K) and background (300 K), $R'(\lambda)$ is normalized relative spectral response, $M(\lambda, T_{BB})$ is blackbody radiation energy. The Eq. (2-2) indicates the radiance of difference of blackbody light source and background light source. The π factor is taking into account that blackbody light source and background light source are Lambertian Radiators. The absolute spectral response can be obtained by absolute peak responsivity multiplying by normalized relative spectral response.

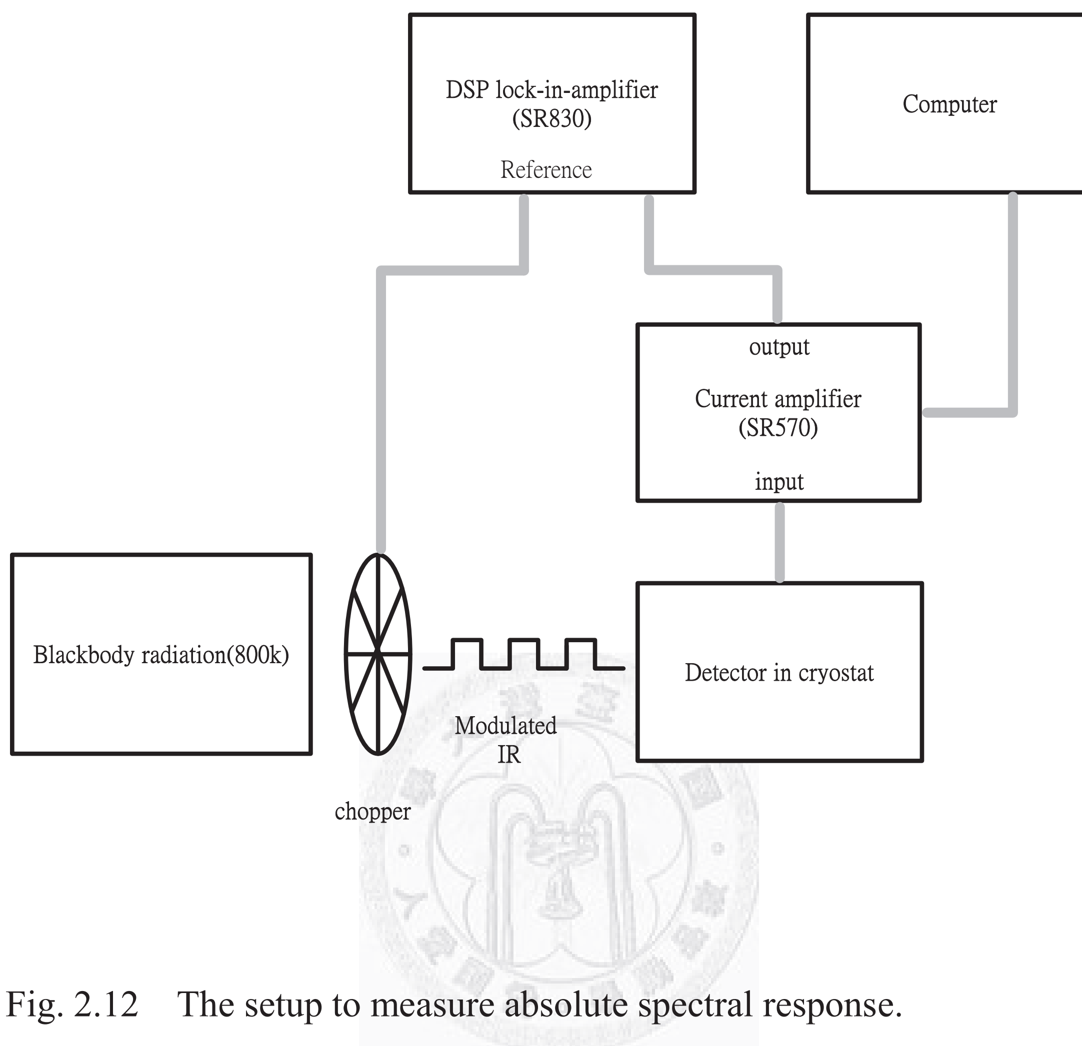

Fig. 2.12 The setup to measure absolute spectral response.

2.3.5 Specific Detectivity

Detectivity is the signal to noise ratio (SNR). The larger SNR, the better device is. The more useful figure of merit is the normalized detectivity D*, which normalizes the detector area and bandwidth

$$D^* = \frac{R_p\sqrt{A_d \Delta f}}{i_n} \qquad (2\text{-}3)$$

Where R_p is the responsivity of the detector, A_d is the area of the detector, Δf is the bandwidth of the measurement and i_n is the noise current, which is attributed to the shot noise. It can be expressed as

$$i_n = \sqrt{4eI_d g_n \Delta f} \qquad (2\text{-}4)$$

The advantage of D* as a figure of merit is that it is normalized to an active detector area of 1 cm^2 and noise bandwidth of 1 Hz. Therefore, D* may be used to compared directly the merit of detectors of different size whose performance was measured using different bandwidths.

2.4 Edge Thinning Introduction

Edge thinning is the structure which reduces the surface leakage current by pinching off surface depletion region and junction depletion region in the edge. It was facilitated on heterojunction bipolar transistor to reduce the surface recombination and consequently enhance the current gain. In this work, edge thinning structure is adopted to reduce the surface leakage current of quantum dot infrared photodetector (QDIP) and consequently enhance its operation temperature.

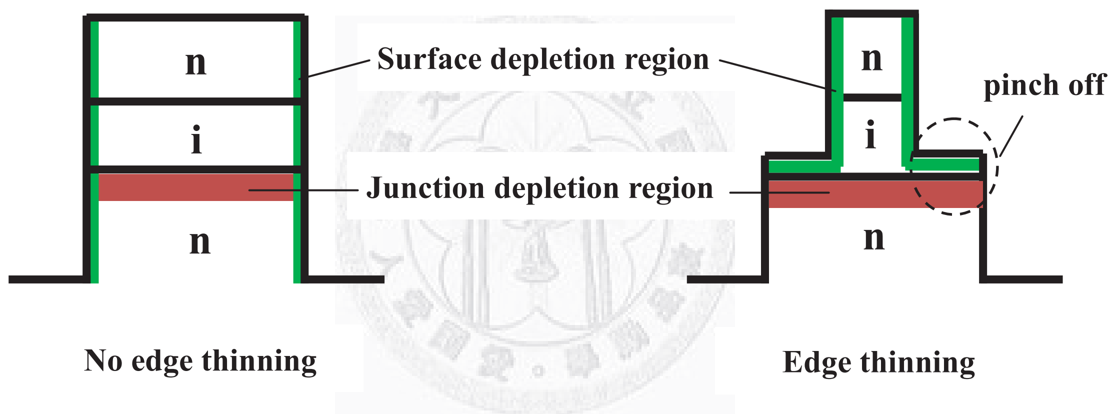

Fig. 2.13 The pinching off mechanism of edge thinning structure.

As Fig. 2.13 shows, the profile of surface depletion region is different between devices with edge thinning structure and those without because of the profile of surface edge. In device with edge thinning structure, the junction depletion region and the surface depletion region may pinch off in the edge and consequently block the path of surface leakage current. As a result, the surface leakage current may be reduced and the operation temperature could be enhanced.

The thickness of junction depletion region can be

$$x_{juntion} = \left\{ \frac{2 \in_S V_{bi}}{e} \left[\frac{N_d}{n_i} \right] \left[\frac{1}{n_i + N_d} \right] \right\}^{1/2}$$

Where ε_S is the dielectric constant; V_{bi}, the built-in potential ; e, the electronic charge; N_d, the n-type doping concentration; n_i , the intrinsic carrier concentration.

The thickness of surface depletion region can be evaluated by the minority carrier hole concentration as a function of distance from the surface.

$$\delta p(x) = g' \tau_{p0} \left(1 - \frac{sL_p e^{-x/L_p}}{D_p + sL_p} \right)$$

The parameter s is called the surface recombination velocity ; g', the generation rate of the excess carrier; τ_{po}, the excess minority carrier lifetime; D_p ,the diffusion coefficient of the excess minority carrier; L_P , the diffusion length of the excess minority carrier. The thickness of surface depletion region can be evaluated as the distance from the transition point of the steady state of $\delta p(x)$ to the surface.

The appropriate thickness of edge thinning structure is supposed to be close to the sum of the thickness of junction depletion region and the surface depletion region so that they can pinch off and consequently block the surface leakage current.

2.5 Atomic Layer Deposition Mechanism and the transmission of Al_2O_3 in the infrared spectrum

In air H_2O vapor is adsorbed on most surfaces, forming a hydroxyl group. After placing the substrate in the reactor, Trimethyl Aluminum (TMA) is pulsed into the reaction chamber as Fig. 2.14 (a). Then, Trimethyl Aluminum (TMA) reacts with the adsorbed hydroxyl groups, producing methane (CH_4) as the reaction product as shown in Fig. 2.14 (b). Trimethyl Aluminum (TMA) will react with the adsorbed hydroxyl groups, until the surface is passivated. However, TMA does not react with itself, terminating the reaction to one layer. This causes the perfect uniformity of ALD. Then, the excess TMA is pumped away with methane reaction product as Fig. 2.14 (c). After the TMA and methane reaction product is pumped away, water vapor (H_2O) is pulsed into the reaction chamber again as Fig. 2.14 (d). H_2O will react with the dangling methyl groups on the new surface forming aluminum-oxygen (Al-O) bridges and hydroxyl surface groups, and waiting for a new TMA pulse. The reaction product methane is pumped away again as Fig. 2.14 (e). However, excess H_2O vapor does not react with the hydroxyl surface groups, again causing perfect passivation to one atomic layer as Fig. 2.14 (f). One TMA and one H_2O vapor pulse form one cycle, with approximately 1 Angstrom per cycle. Each cycle including pulsing and pumping takes

3 seconds as Fig. 2.14 (g). Since each pair of gas pulses (one cycle) produces exactly one monolayer of film, the thickness of the resulting film may be precisely controlled by the number of deposition cycles. Figs. 2.14 (a) to (g) show the Al_2O_3 forming process sequences.

Fig. 2.15 shows the transmission of GaAs substrate (S.I) and GaAs with 10-nm-thick Al_2O_3 layer deposited by ALD in the infrared spectrum. Obviously, the transmission of GaAs substrate and GaAs with Al_2O_3 layer in the infrared spectrum are similar. It means that the Al_2O_3 layer does not absorb infrared light. Hence, the Al_2O_3 layer deposited by ALD doesn't block the QDIPs' absorbsion of infrared light.

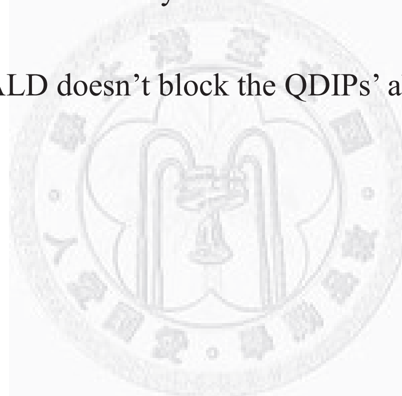

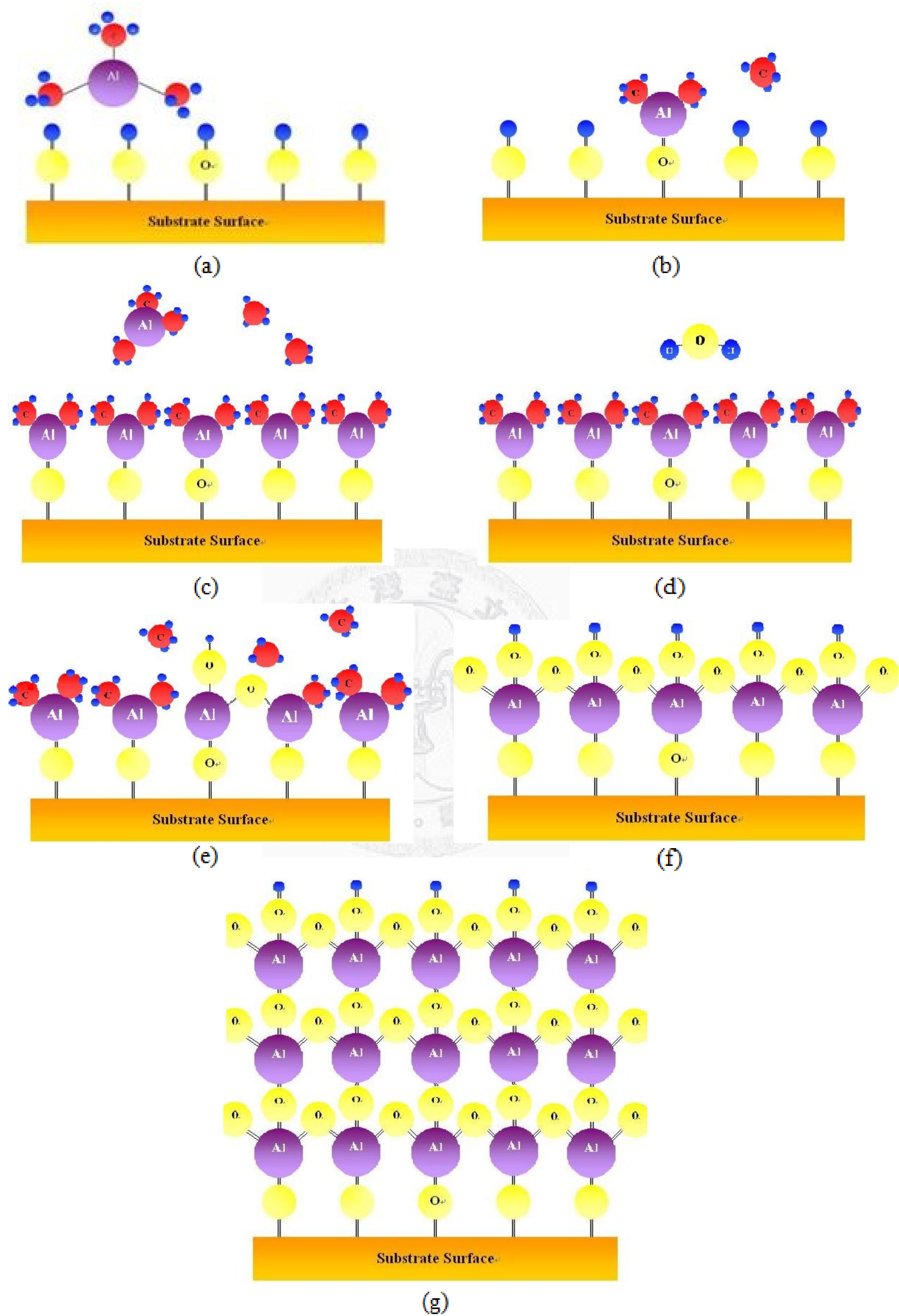

Fig. 2.14 The Al_2O_3 layer forming process sequence.

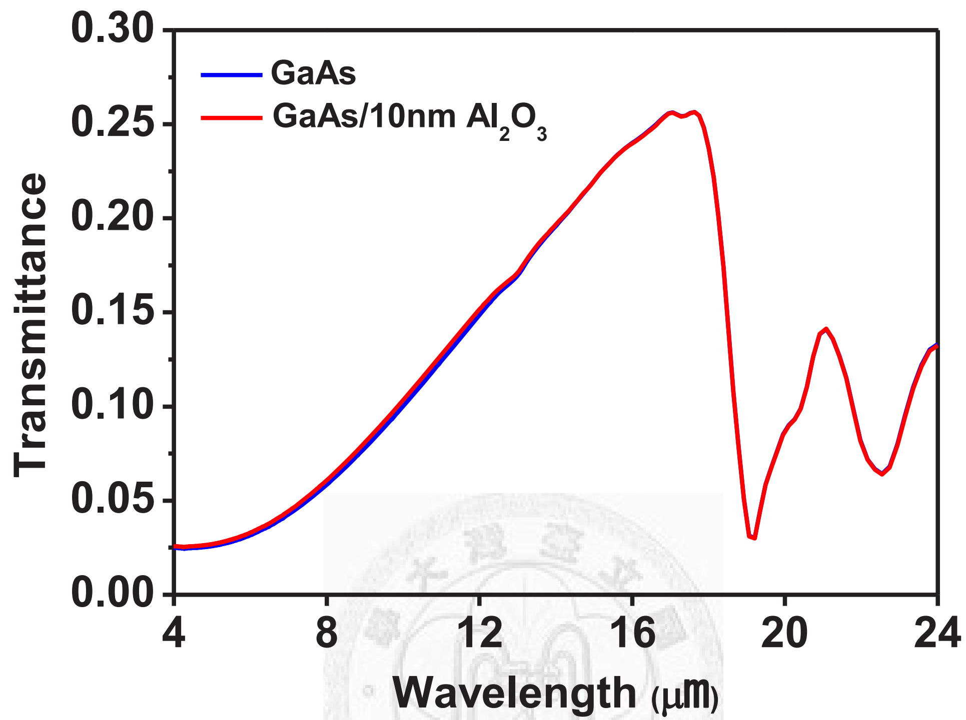

Fig. 2.15 The transmission of GaAs and GaAs with Al_2O_3 layer in the infrared spectrum.

Chapter 3 Edge Thinning Structure with Different Depths on QDIPs

Self-assembled InAs quantum dots (QDs) on GaAs substrate using Stranski-Ḱrastanov (SK) growth mode by molecular beam epitaxy (MBE) have attracted much attention in recent years [38-39]. Due to its long capture and relaxation times, the QD structure is suitable for the optoelectronic applications of the infrared photodetectors [40-42], lasers [43], and optical memories [44]. The fabrication of QDIPs has attracted growing interest recently [45-47]. Although the advantages such as high-temperature operation and insensitivity to incident light polarization have made QDIPs superior than quantum-well infrared photodetectors (QWIPs) for applications. It still needs lots of efforts to achieve room temperature operation.

In this work, the edge thinning structure is adopted to reduce the dark current and enhance the operation temperature. In this chapter, the edge thinning structure with different depths on QDIPs will be investigated.

3.1 The Effect of Edge Thinning Structure with Different Depths on IV Characteristics of QDIPs

3.1.1 Sample Preparation

The samples investigated in this article named QDIP75 were grown on (100)-oriented semi-insulating GaAs substrates using a Riber Compact 21 solid-source molecular-beam epitaxy (MBE) system. The device structure is shown in Fig. 3.1 The active region consists of ten periods of 2.4 ML (monolayer) InAs QD layers separated by 30-nm-thick undoped GaAs barrier layers. 600 and 300 nm n^+ GaAs layers doped with n=2×10^{18} cm^{-3} were grown to sandwich the active region as the bottom and top contact layers.

Three devices are fabricated as shown in Fig. 3.2 (a), (b), (c), respectively. Device A is the standard device without edge thinning structure, which was etched down directly to bottom contact layer in a mesa pattern ($280 \times 180 \mu m^2$) to form bottom ohmic contact. Device B is the device with edge thinning structure at top contact layer, which was first etched down to top contact layer in a mesa pattern ($280 \times 180 \mu m^2$) and then further etched down to bottom contact layer in a larger mesa pattern ($300 \times 200 \mu m^2$) to form bottom ohmic contact. Device C is the device with edge thinning structure at quantum dot layer, which was first etched down to quantum dot layer in a mesa pattern ($280 \times 180 \mu m^2$) and then further etched down to

the bottom contact layer in a larger mesa pattern ($300 \times 200\mu m^2$) to form bottom ohmic contact. The thicknesses of the edge structure are between 100nm~200nm.

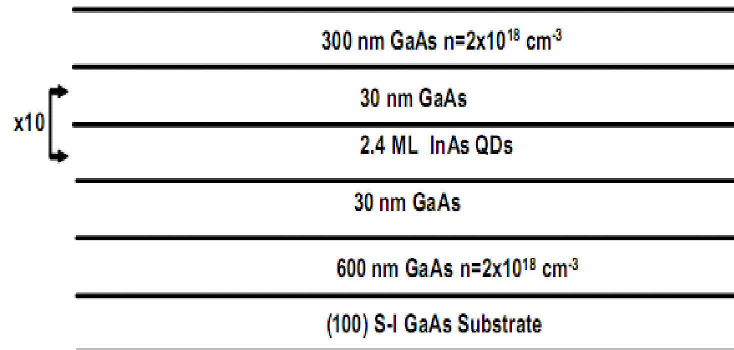

Fig. 3.1 The schematic diagram of device structure (QDIP75).

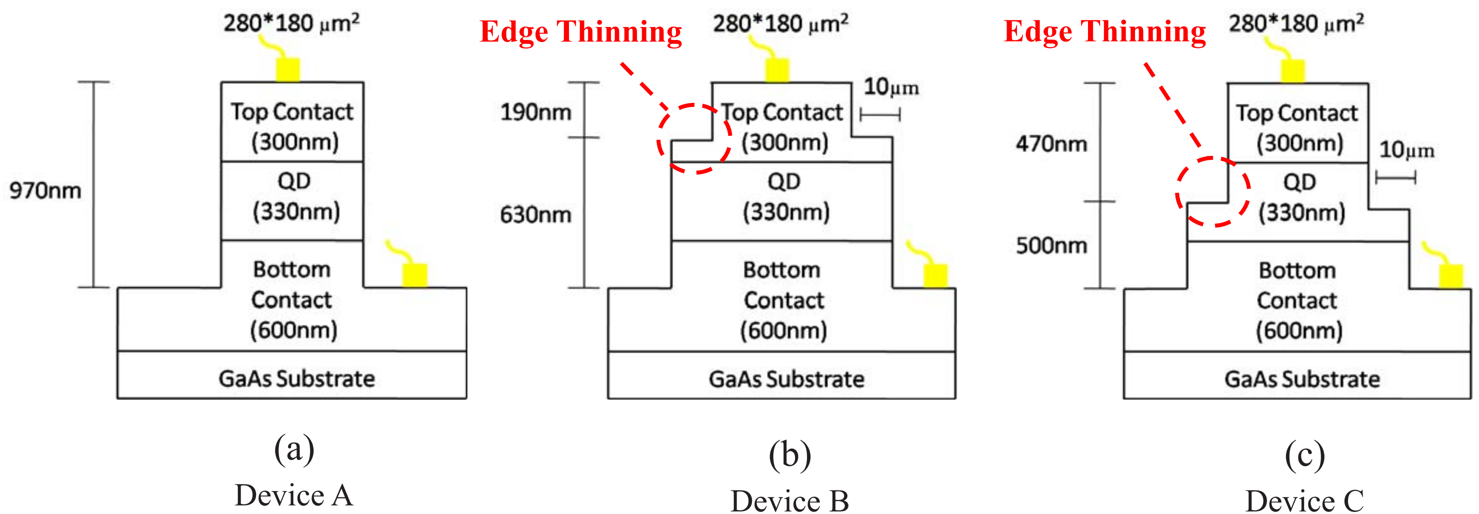

(a)
Device A

(b)
Device B

(c)
Device C

Fig. 3.2 The schematic diagram of devices (a) A, the standard device without edge thinning structure, (b) B, the device with edge thinning structure at top contact layer, (c) C, the device with edge thinning structure at quantum dot layer.

3.1.2 Results and Discussion

Figs. 3.3 to 3.5 show the I-V characteristics of devices A (without edge thinning structure), B (with edge thinning structure at top contact) and C (with edge thinning structure at quantum dot layer), respectively. The background limited performance (BLIP) of all devices can be reckoned as 70 K. Fig 3.6 (a) and (b) show the comparison of dark I-V characteristics of devices A, B, and C at 20 K and 90 K respectively. At 20 K, the dark current of devices B and C are very similar. The dark current of both devices B and C are about two orders of magnitude lower than that of device A at bias voltage from about -0.8V to -1.3V. It's because of the natural discrepancy in the sample. At bias voltage beyond 1.6V and below -1.5V, the dark current of devices B and C exceed that of device A. It's because the cross section area of bottom contact and the surface area of devices B and C is larger than that of device A so the dark current could be larger. At 90 K, the dark current characteristics of devices A, B and C are similar also.

In summary, the adopted edge thinning structure doesn't have significant effect on the dark I-V characteristics of QDIPs in this experiment.

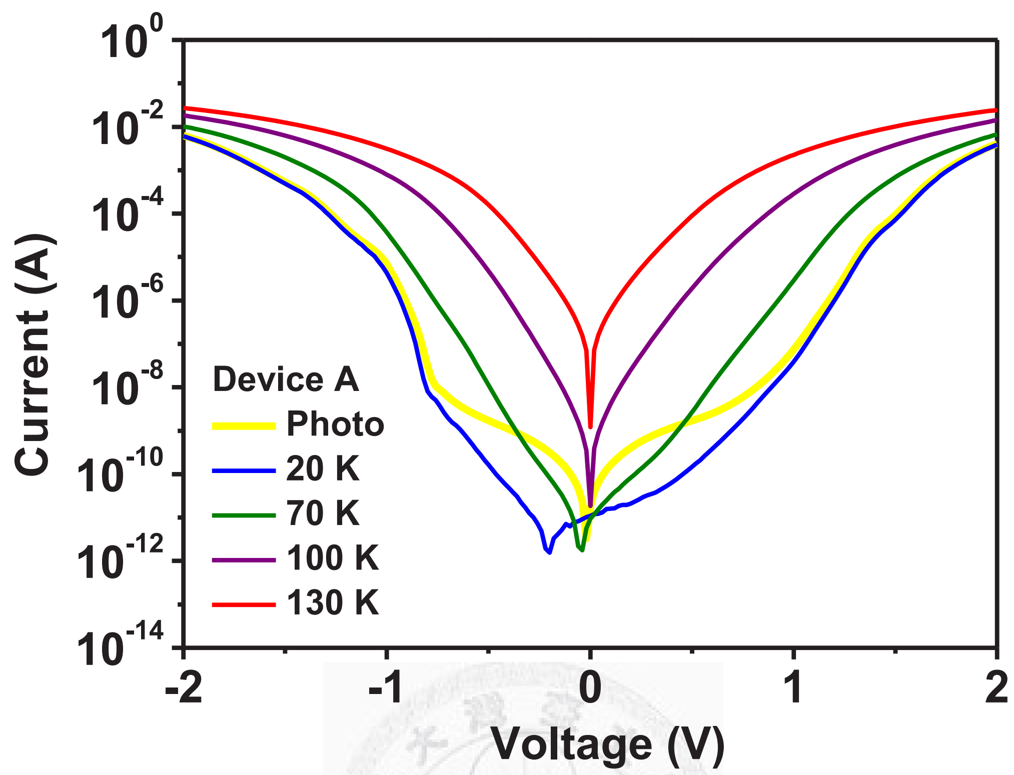

Fig. 3.3 The I-V characteristic of device A.

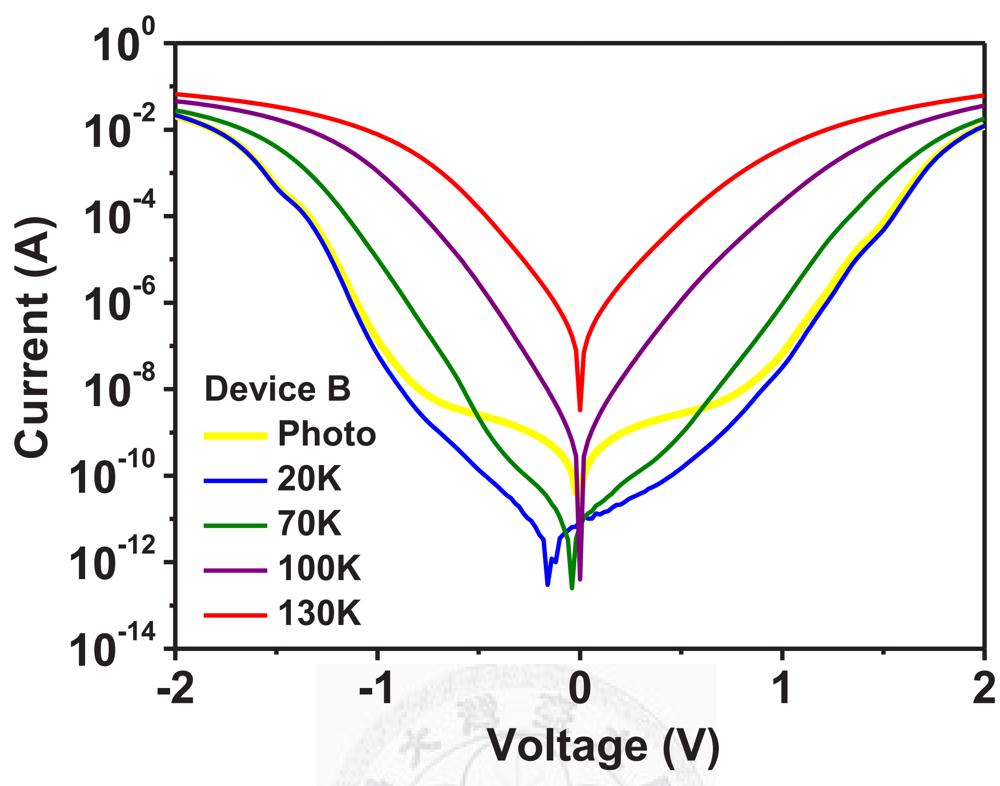

Fig. 3.4 The I-V characteristic of device B.

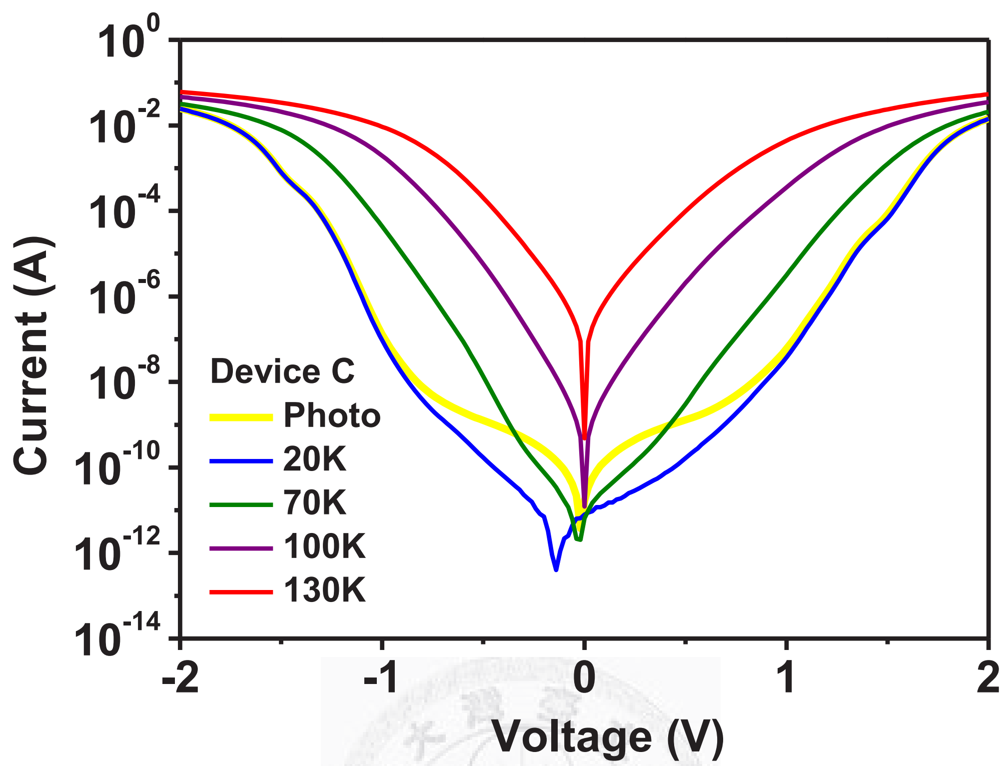

Fig. 3.5 The I-V characteristic of device C.

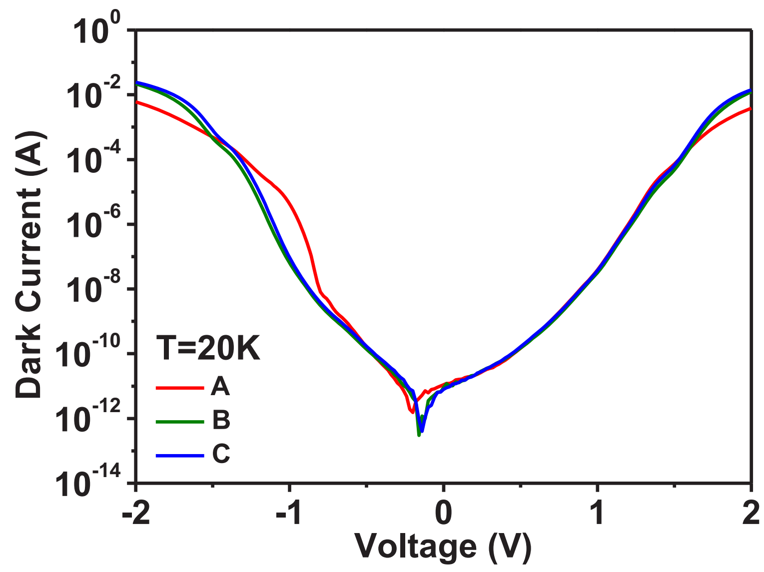

(a)

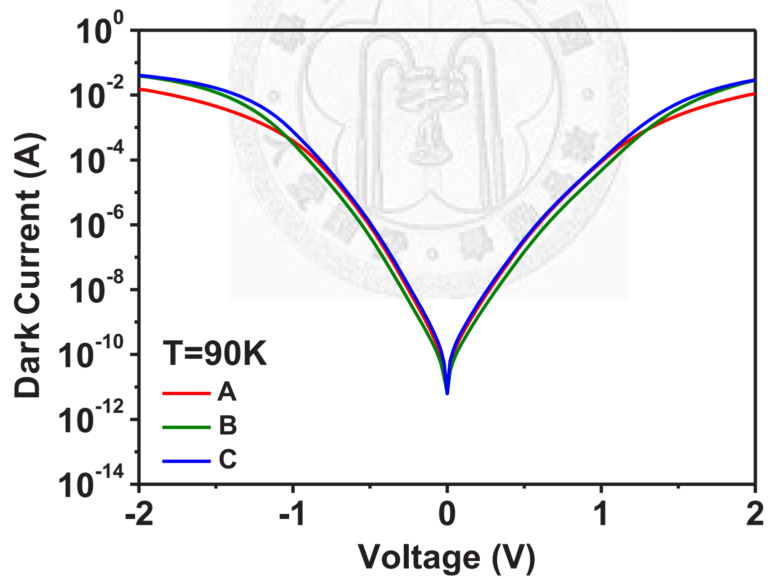

(b)

Fig. 3.6 The comparison of dark I-V characteristics of devices A, B , and C at T= (a) 20 K and (b) 90 K.

3.2 The Effect of Edge Thinning Structure with Different Depths on photo-response of QDIPs

3.2.1 Sample Preparation

The devices A, B, and C investigated in this section are the same as those in section 3.1. The schematic diagram of sample structure and device structure are shown in Fig 3.1 and Fig 3.2 respectively.

3.2.2 Results and Discussion

Figs. 3.7 to 3.9 show the photo-response of devices A, B and C, respectively. The operation temperature of device A is 120 K. On the other hand, the operation temperature of devices B and C are both 125 K. The operation temperature of devices A, B and C are close. In this experiment, the adopted edge thinning structure doesn't enhance the operation temperature of QDIPs.

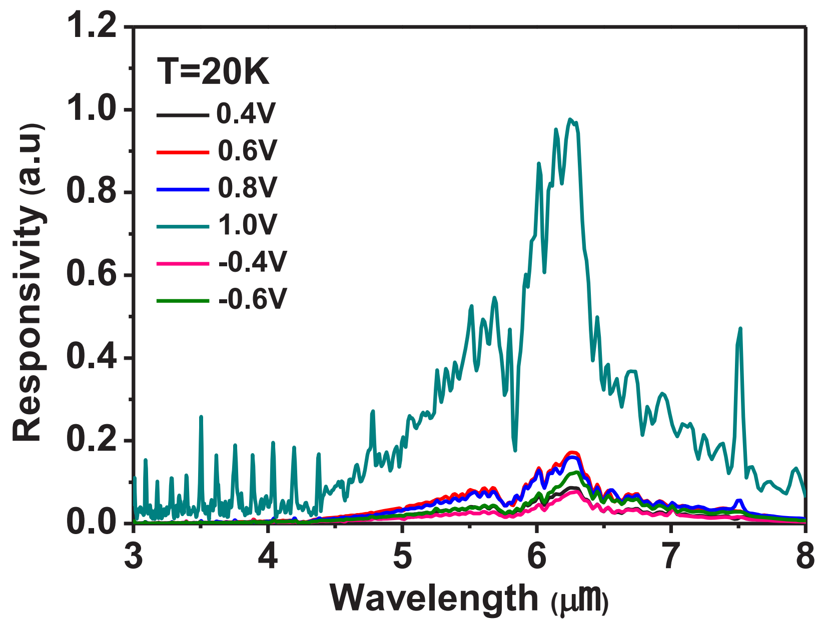

(a)

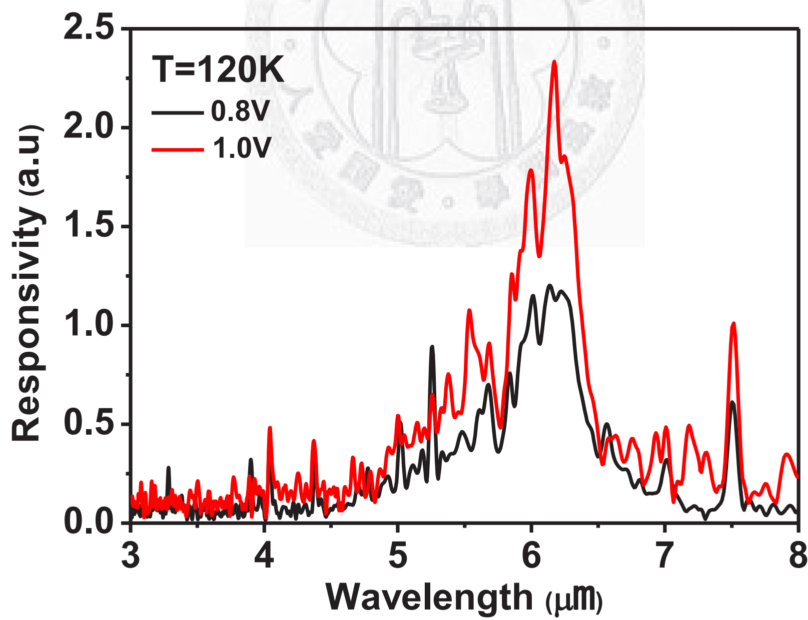

(b)

Fig. 3.7 The responsivities of device A at T= (a) 20 K and (b) 120 K (the highest operation temperature) at different biases.

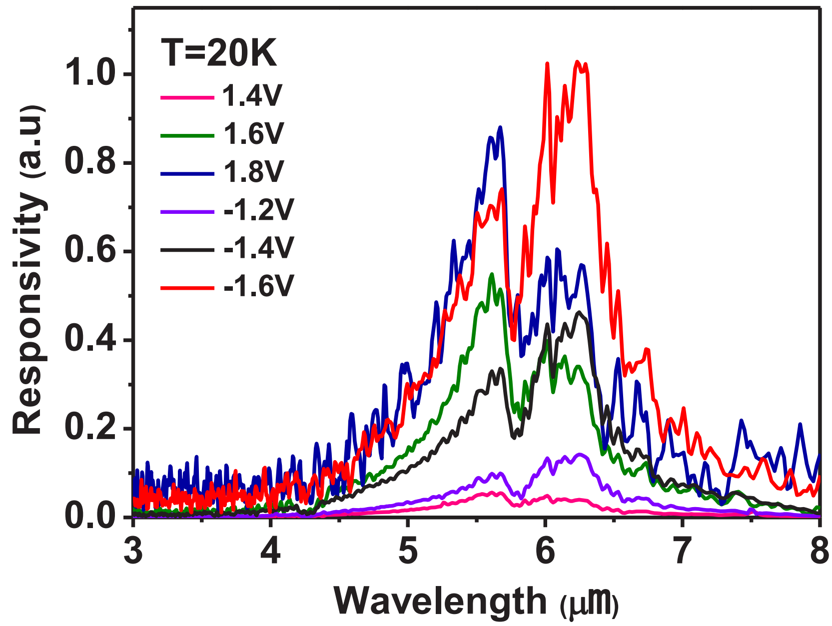

(a)

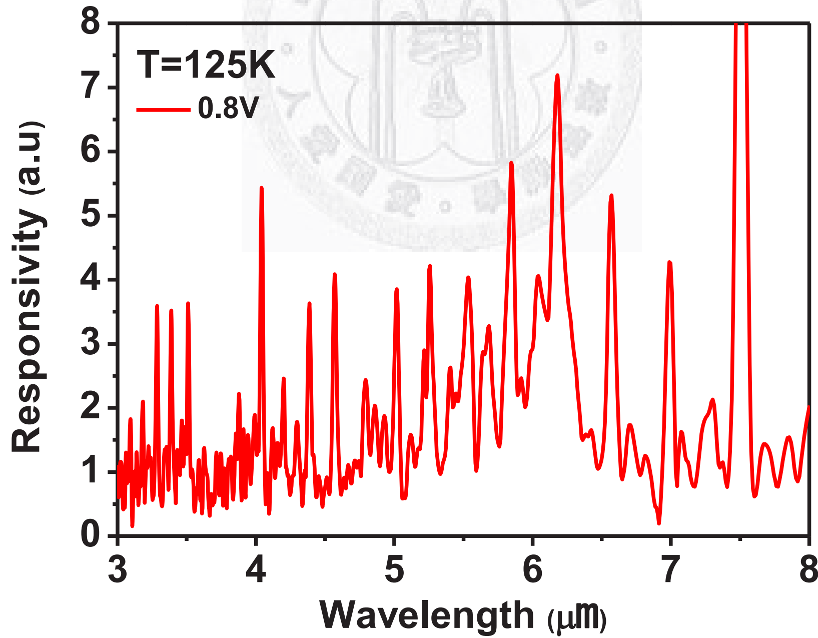

(b)

Fig. 3.8 The responsivities of the device B at T= (a) 20 K and (b) 125 K (the highest operation temperature) at different biases.

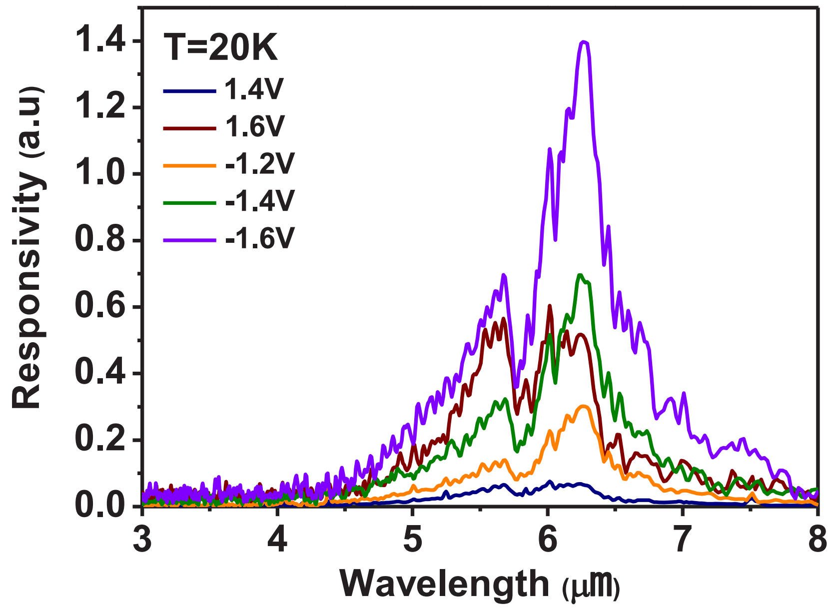

(a)

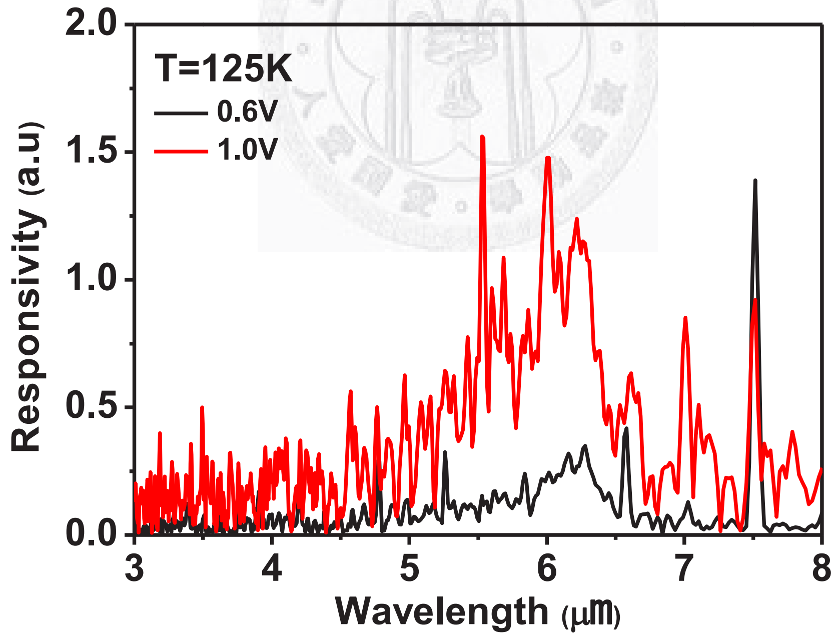

(b)

Fig. 3.9 The responsivities of device C at T= (a) 20 K and (b) 125 K (the highest operation temperature) at different biases.

Chapter 4 The Combination of Edge Thinning Structure and Surface Passivation Layer on the Performance of QDIPs

The combination of edge thinning structure and surface passivation by atomic layer deposition on the the performance of QDIPs is investigated in this chapter. Lai et al. [12] has discovered that surface passivation by atomic layer deposition of Al_2O_3 can also effectively reduce surface leakage current and elevate operation temperature. Therefore, the combination of edge thinning structure and surface passivation is adopted in this chapter to block the surface leakage current of QDIPs and achieve higher operation temperature.

4.1 Sample Preparation

The sample investigated in this chapter is QDIP75. The schematic device structure of device D, the standard device with surface passivation layer Al_2O_3, device E, with edge thinning at top contact layer and surface passivation layer Al_2O_3, and device F, with edge thinning at quantum dot layer and surface passivation layer Al_2O_3 are shown in Fig. 4.1 (a) and (b), respectively. The fabrication process of the device is shown in Fig. 4.2 After the edge thinning structure formation as indicated in Fig. 2.5 (a)~(h), the samples were dipped into diluted HF (1%) solution for 1 minute and followed by diluted NH_4OH (10%) solution for 1minute. The HF treatment can remove the native oxide and the NH_4OH treatment can leave the surface-OH terminated which may ensure better quality of Al_2O_3 layer. Then the samples were immediately transferred to an ALD reactor for Al_2O_3 deposition.10nm of Al_2O_3 dielectric material deposited by Atomic Layer Deposition (ALD) at 300° C was used to coat the mesa edges surrounding the QDIP. Then the RTA process was used to eliminate the fixed oxide charges at the surface between QDIP and Al_2O_3 layer. The annealing rate is 200 ^{o}C/min up to the temperature of 550 ^{o}C and last for 5 minutes. Then the third photolithography step was used to define the region for ohmic contact. After the third photolithography step, 20 minutes hard baking was used to formalize the pattern. Then wet etching using of dilute HF ($HF:H_2O$=1:50) to remove the spare

Al_2O_3 which was deposited on the ohmic contact region. The etching time is about 90 seconds. After wet etching process, the Au-Ge-Ni/Au alloy was deposited by thermal evaporation and followed by thermal annealing at 420° C for 2 minutes to form ohmic contacts. Finally, the device with edge thinning structure and surface passivation layer Al_2O_3 are completed.

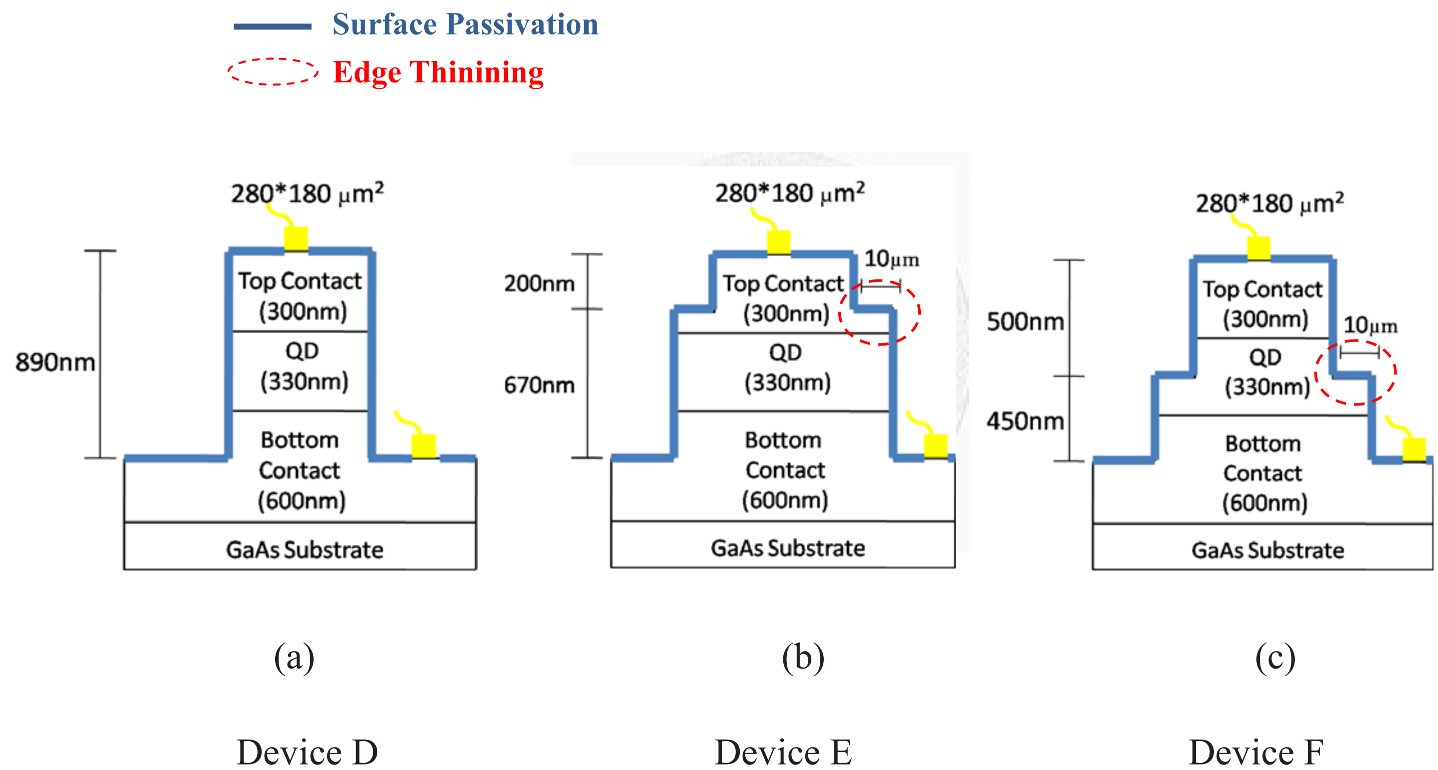

Fig. 4.1 The schematic structure of devices (a) D, the standard device with surface passivation by ALD Al_2O_3, (b) E, the device with edge thinning structure at top contact layer and surface passivation by ALD Al_2O_3, (c) F, the device with edge thinning structure at quantum dot layer and surface passivation by ALD Al_2O_3.

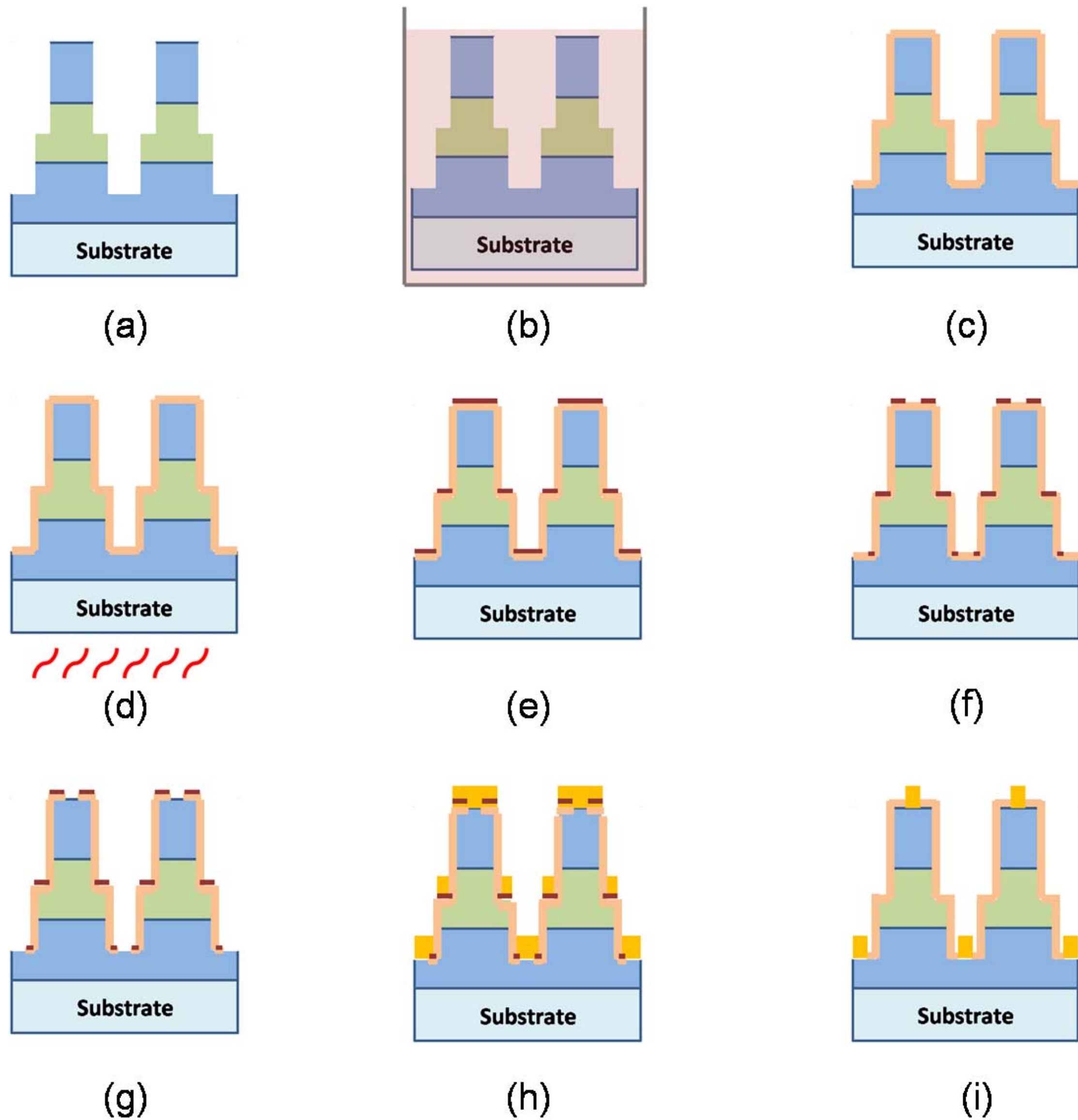

Fig. 4.2 The fabrication processes of devices with edge thinning structure and surface passivation layer, (a) edge thinning structure formation (as Fig. 2.5 (a)-(h) show), (b) dip in HF / NH_4OH, (c) surface passivaiton layer Al_2O_3 by ALD, (d) RTA, (e) photoresist coating, (f) developing, (g) wet etching Al_2O_3 by diluted HF, (h) metals evaporation, (i) lift off.

4.2 Results and Discussion

Figs. 4.3 to 4.5 show the I-V characteristics of devices D, E, and F, respectively. The background limited performance (BLIP) of all devices can be reckoned as 70 K.

Fig. 4.6 (a) and (b) display the comparison of dark I-V characteristics of devices A and D at 20 K and 90 K, respectively. The dark I-V characteristics of devices A and D are similar. Fig. 4.7 (a) and (b) display the comparison of dark I-V characteristics of devices B and E at 20 K and 90 K, respectively. At 20 K, the dark current of device E is 1 order of magnitude lower than that of device B at bias voltage beyond 1.5V and below -1.5V. At 90 K, the dark current of device E is 1 order of magnitude lower than that of device B at bias voltage beyond 1.2V and below -1.0V. Fig. 4.8 (a) and (b) display the comparison of dark I-V characteristics of devices C and F at 20 K and 90 K, respectively. At 20 K, the dark current of device F is 2 orders of magnitude lower than that of device C at bias voltage beyond 1.0V and below -1.0V. At 90 K, the dark current of device F is 2 orders of magnitude lower than that of device C at bias voltage beyond 0.5V and below -0.5V.

Fig. 4.9 (a) and (b) display the comparison of dark I-V characteristics of devices D, E and F at 20 K and 90 K, respectively. At 20 K, the dark current of device F and device E are 2 orders and 1 order of magnitude lower than that of device D , respectively at bias voltage beyond 1.0V and below -1.0V. At 90 K, the dark current

of device F is 1 order of magnitude lower than that of device D at bias voltage beyond 0.5V and below -0.5V and the dark current characteristics of devices E and D are similar.

According to the comparison of dark I-V characteristics, it can be inferred that the dark current reduction effect of surface passivation layer Al_2O_3 combined with edge thinning structure is better than that of surface passivation layer Al_2O_3 only. The surface passivation layer Al_2O_3 combined with edge thinning structure at quantum dot layer can reduce dark current by 2 orders of magnitude, which is the optimum improvement in this experiment.

Fig. 4.10 (a), (b) and (c) display the comparison of photo I-V characteristics of devices A and D, B and E, and C and F, respectively. The photo I-V characteristics of devices A and D are similar. The photo current of device E is 1 order of magnitude lower than that of device B at bias voltage beyond 1.5V and below -1.5V. The photo current of device F is 2orders of magnitude lower than that of device C at bias voltage beyond 1.0V and below -1.0V.

Despite the combination of edge thinning structure and surface passivation layer Al_2O_3 can reduce dark current by 1~2 orders of magnitude, the photo current is also reduced simultaneously.

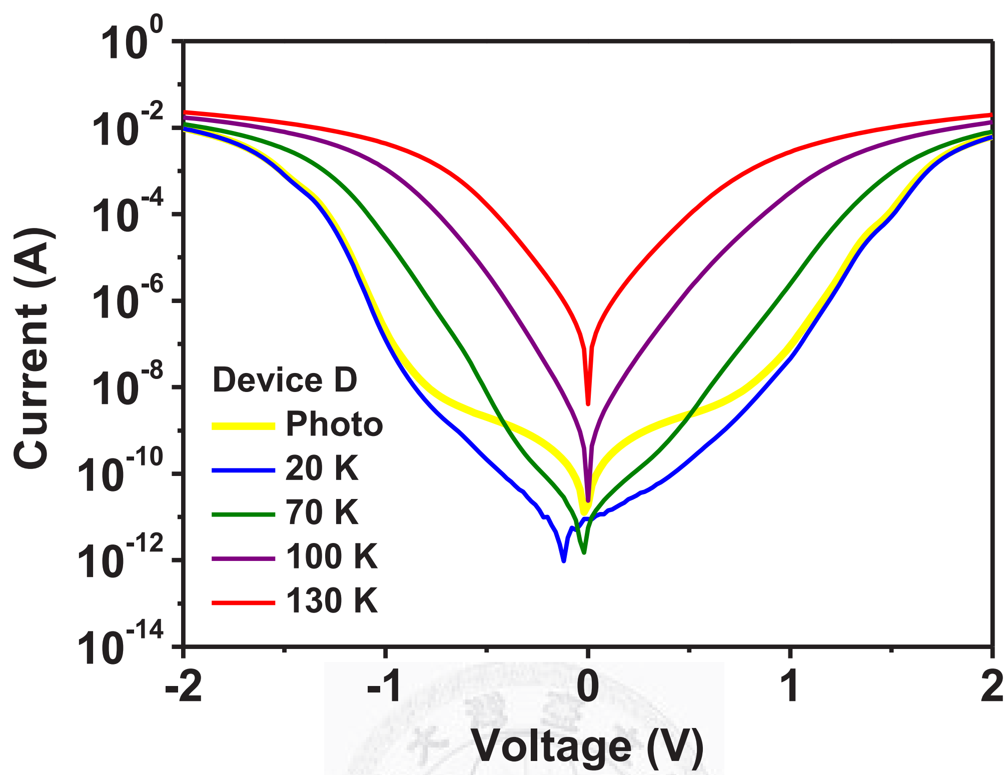

Fig. 4.3 The I-V characteristic of device D.

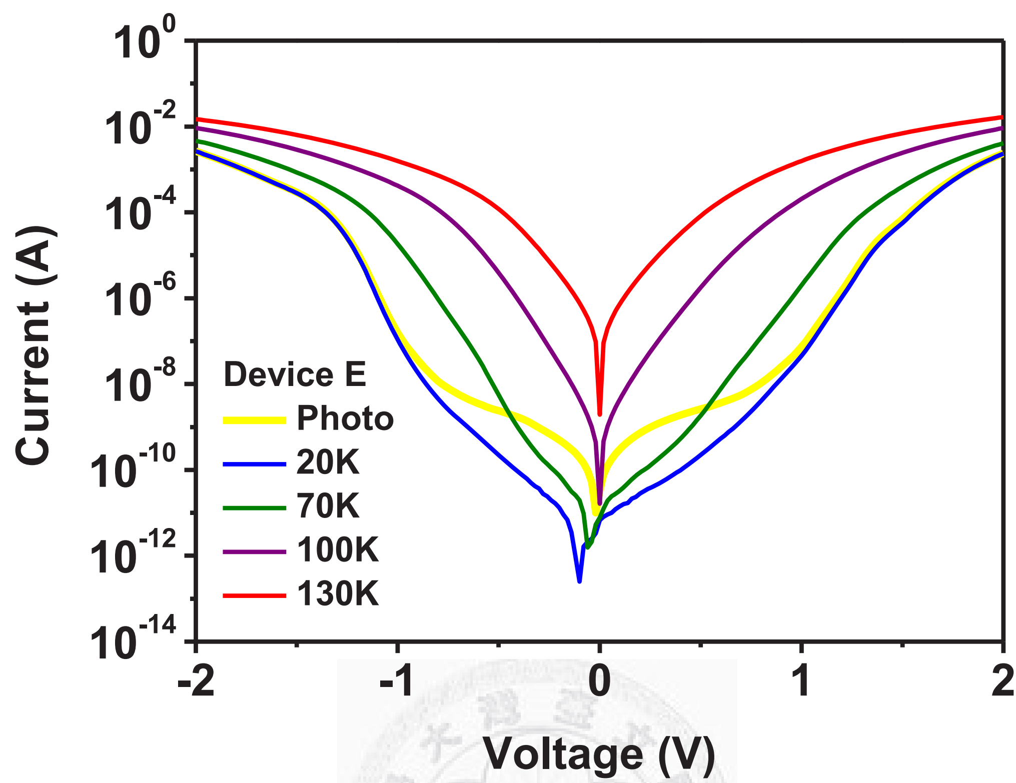

Fig. 4.4 The I-V characteristic of device E.

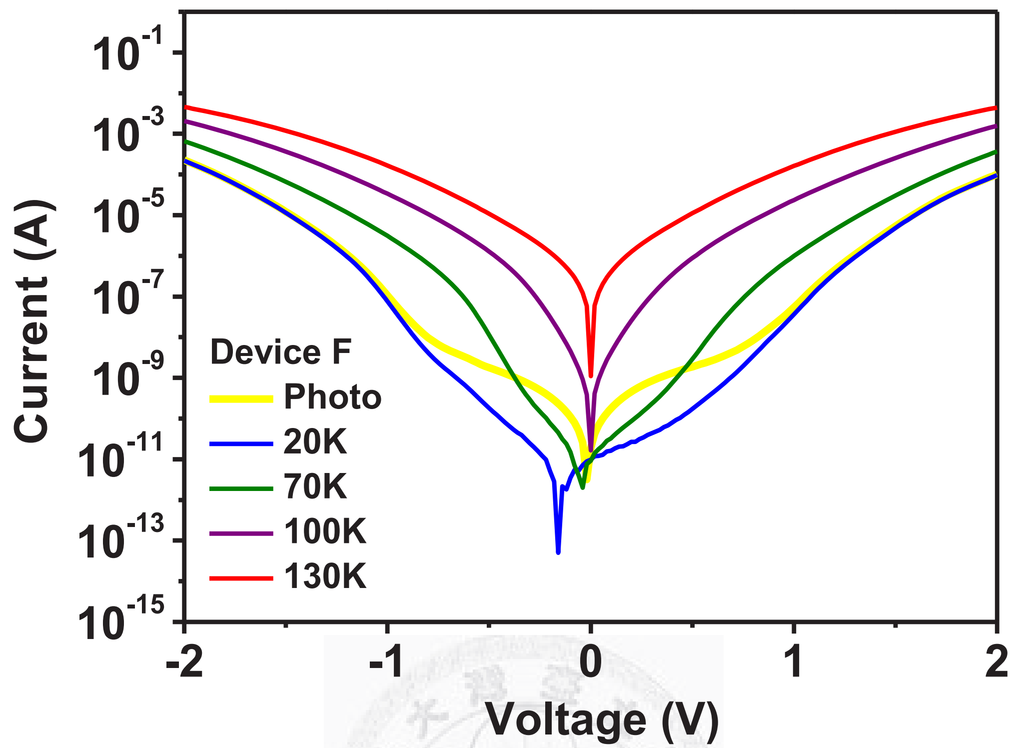

Fig. 4.5 The I-V characteristic of device F.

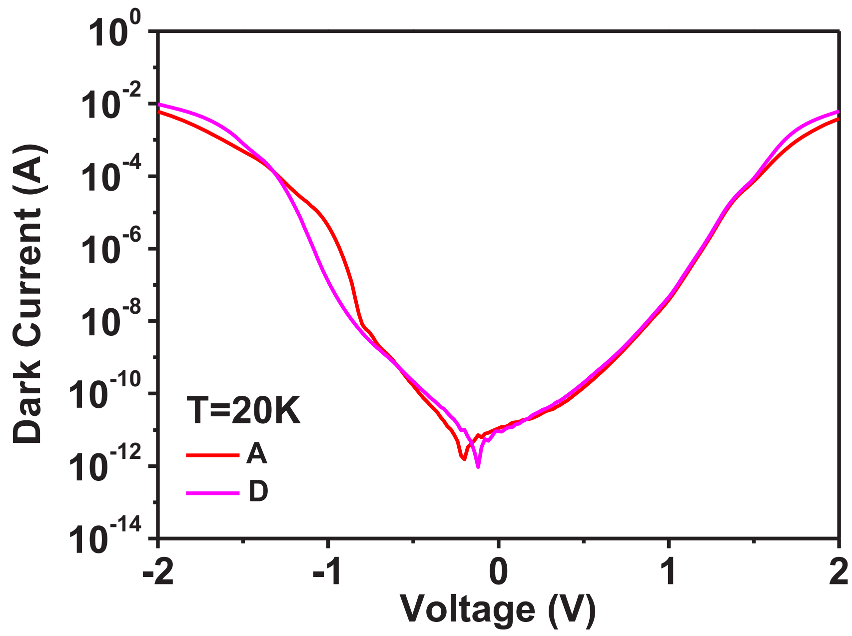

(a)

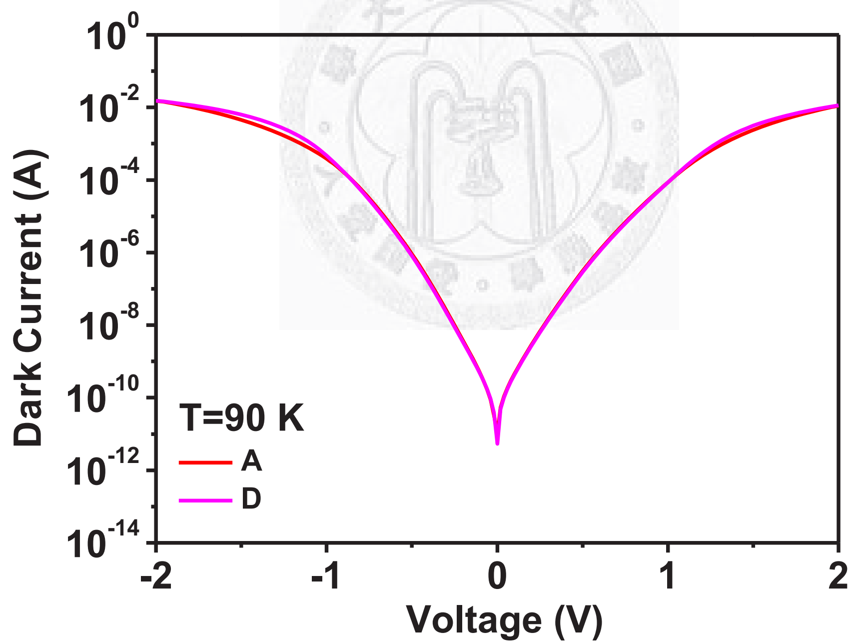

(b)

Fig. 4.6 The comparison of dark I-V characteristics of devices A and D at T= (a) 20 K and (b) 90 K.

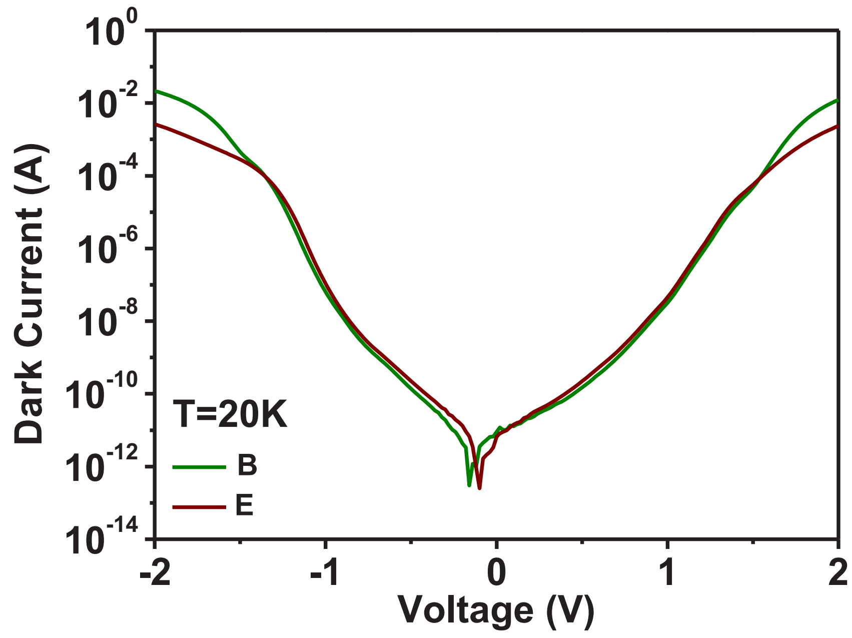

(a)

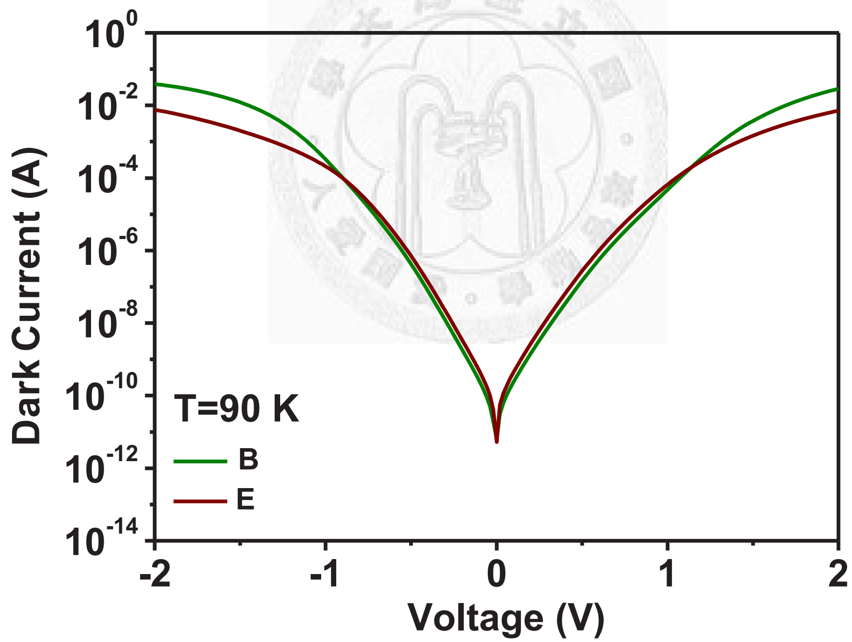

(b)

Fig. 4.7 The comparison of dark I-V characteristics of devices B and E at T= (a) 20 K and (b) 90 K.

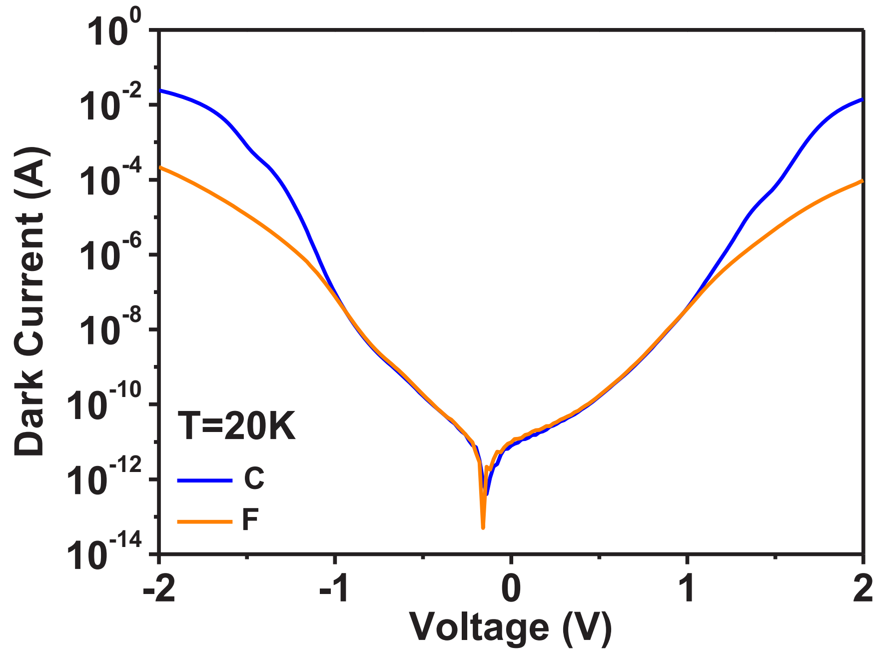

(a)

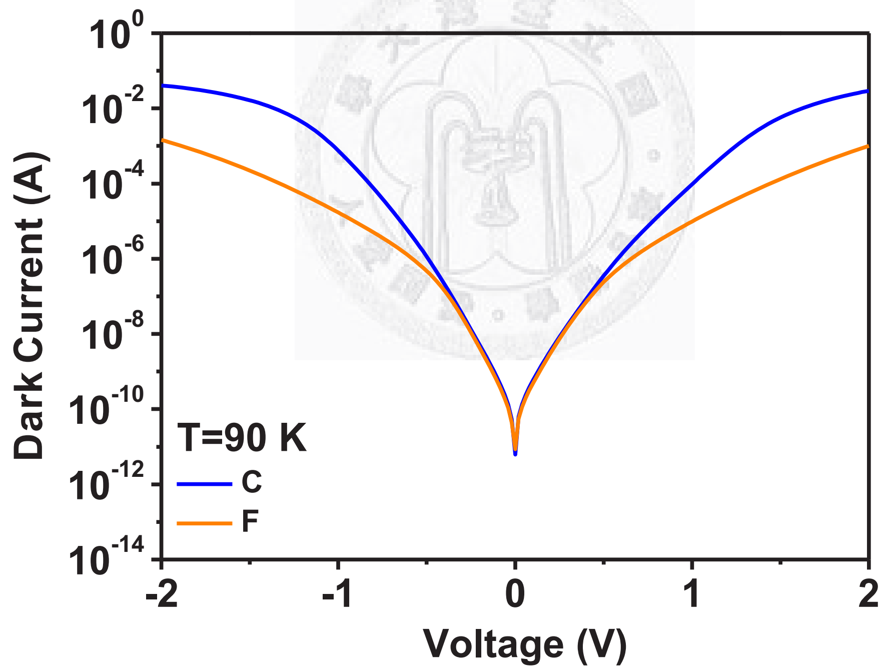

(b)

Fig. 4.8 The comparison of dark I-V characteristics of devices C and F at T= (a) 20 K and (b) 90 K.

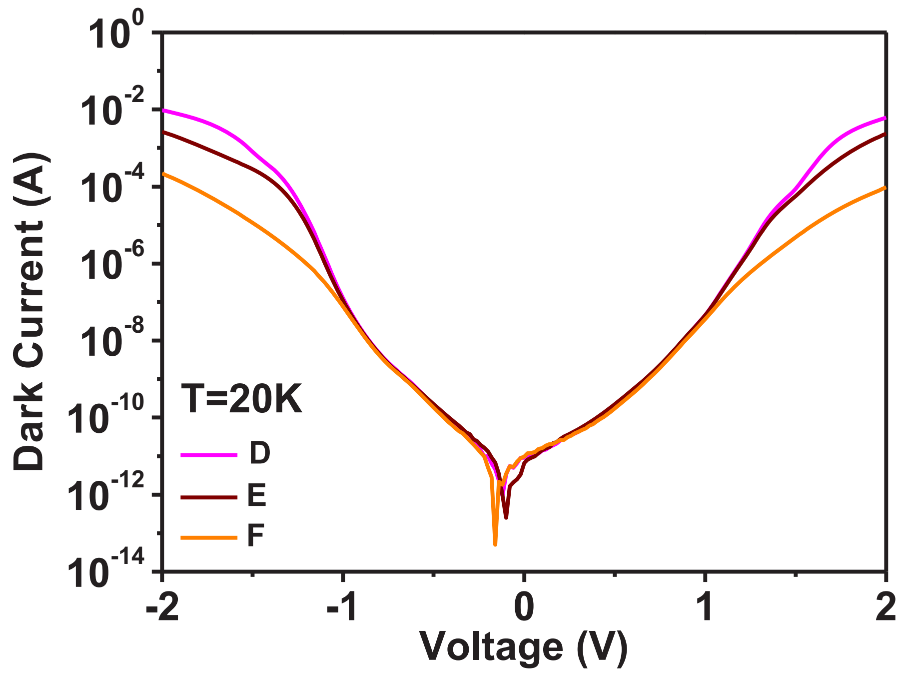

(a)

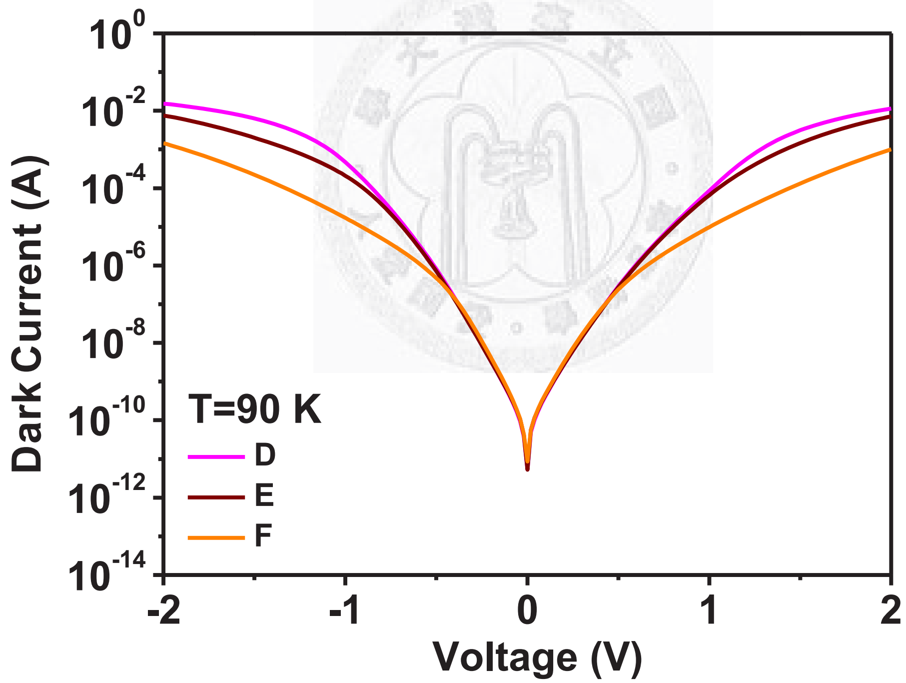

(b)

Fig. 4.9 The comparison of dark I-V characteristics of devices D, E, and F at T= (a) 20 K and (b) 90 K.

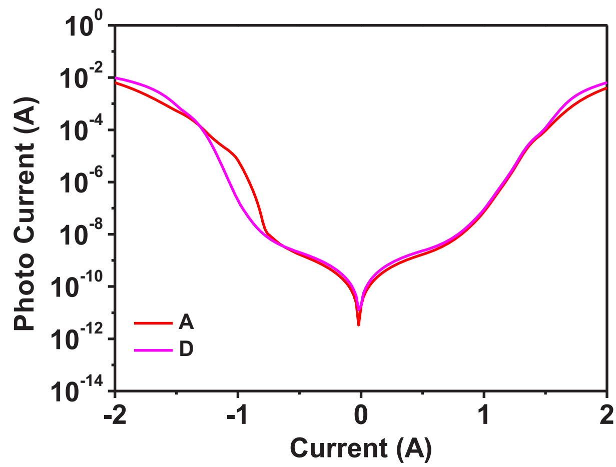

(a)

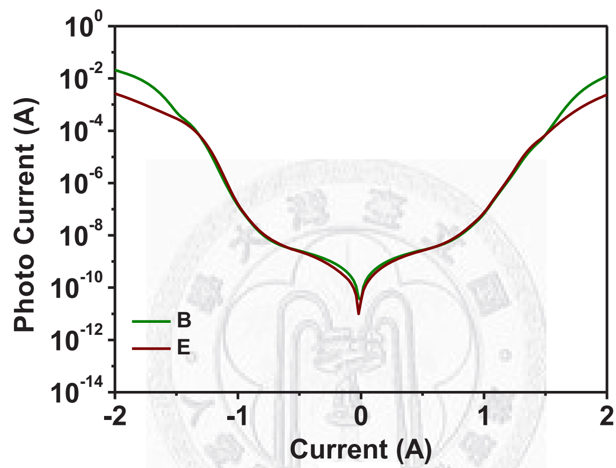

(b)

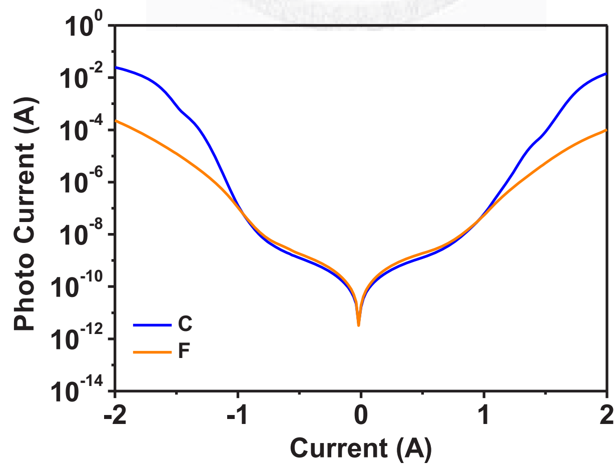

(c)

Fig. 4.10 The comparison of photo I-V characteristics of devices (a) A and D, (b) B and E, and (c) C and F at T=20 K.

Figs. 4.11 to 4.13 (a) and (b) display the responsivities of devices D, E and F at 20 K and the highest operation temperature, respectively. The operation temperature of devices D, E and F are 130 K, 105 K and 135 K, respectively, which are all close to that of device A, 120 K. It can be inferred that the combination of edge thinning structure and surface passivation layer Al_2O_3 doesn't significantly improve the operation temperature of QDIPs in this experiment.

On the other hand, at 20 K, Device F can work at broader bias voltage range (-2.6V~2.6V) than Device A does (-0.8V~1.8V). It's because the current at higher bias voltage is reduced by the combination of edge thinning structure at QD layer and surface passivation layer Al_2O_3.

Fig. 4.14 (a) and (b) display the detectivities of devices A and F at bias voltage = 0.6V and 1.6V, respectively. In both bias voltages, the detectivities of devices A and F are close to each other. It can be inferred that the combination of edge thinning structure and surface passivation layer Al_2O_3 doesn't significantly improve the detectivity of QDIPs in this experiment.

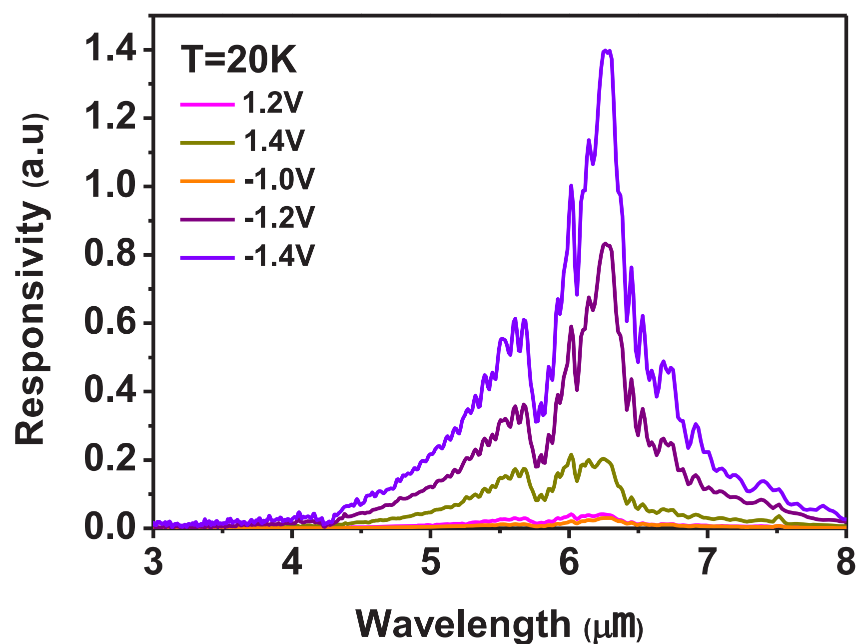

(a)

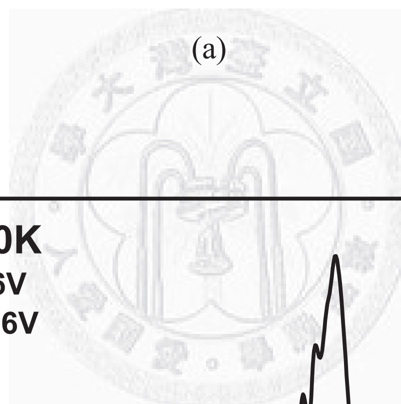

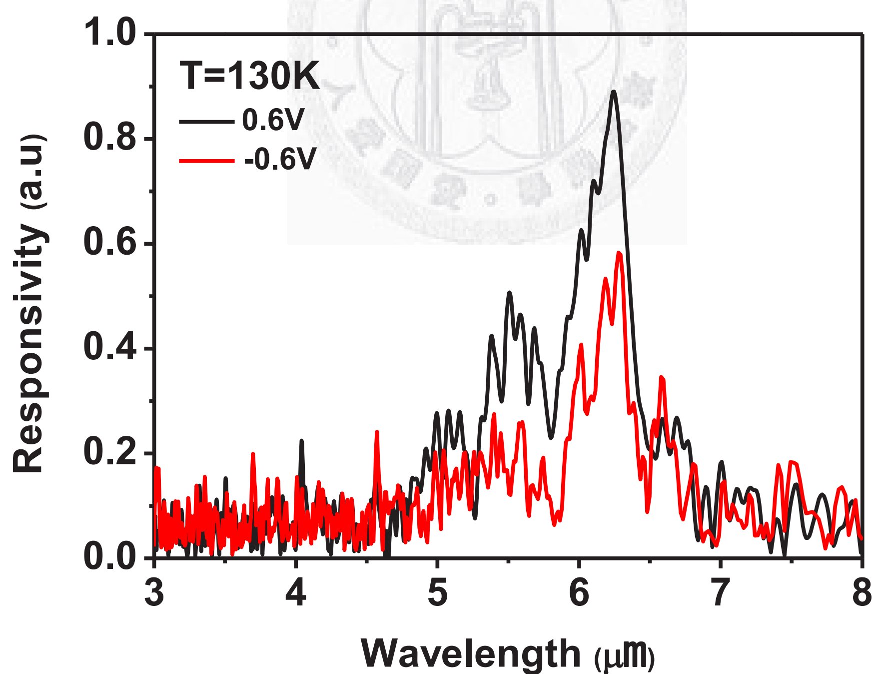

(b)

Fig. 4.11 The responsivities of device D at T= (a) 20 K and (b) 130 K (the highest operation temperature) at different biases.

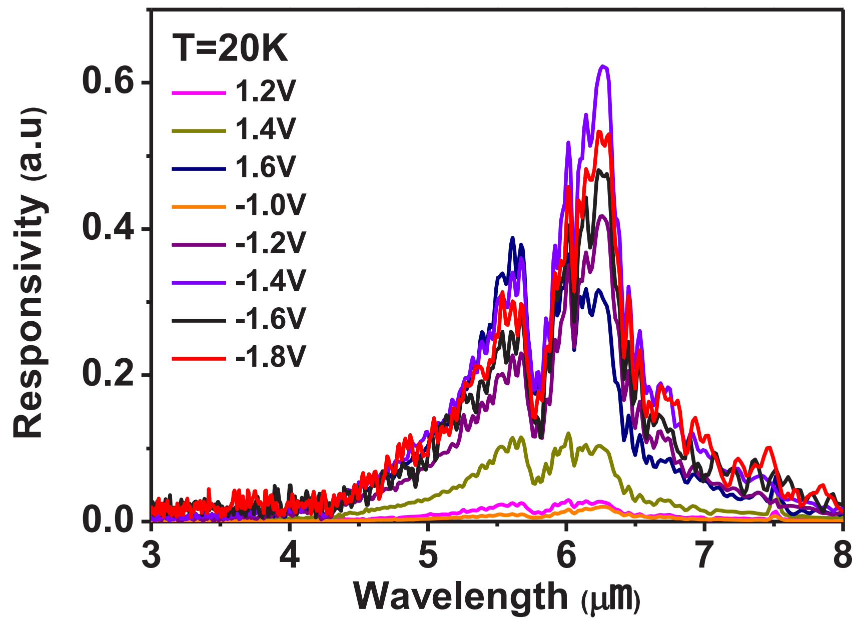

(a)

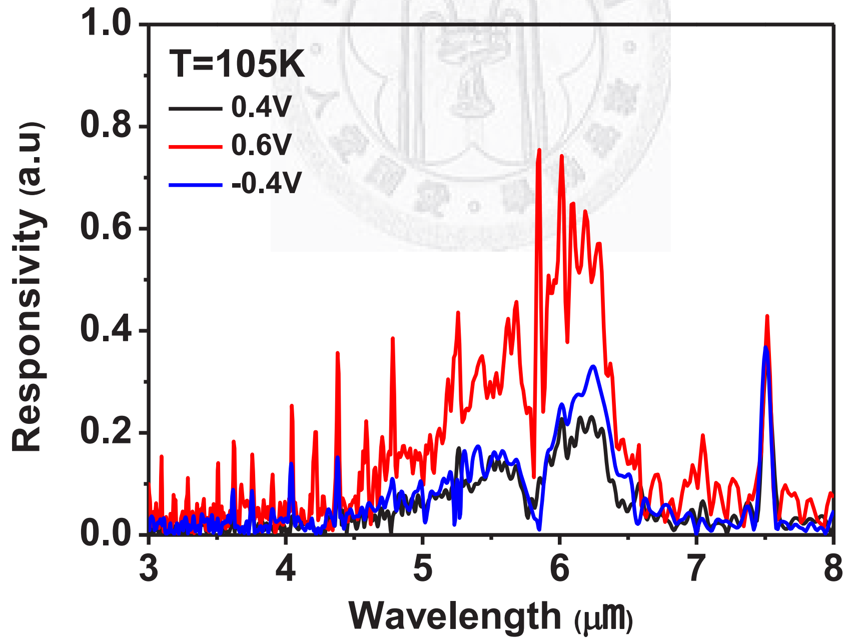

(b)

Fig. 4.12 The responsivities of device E at T= (a) 20 K and (b) 105 K (the highest operation temperature) at different biases.

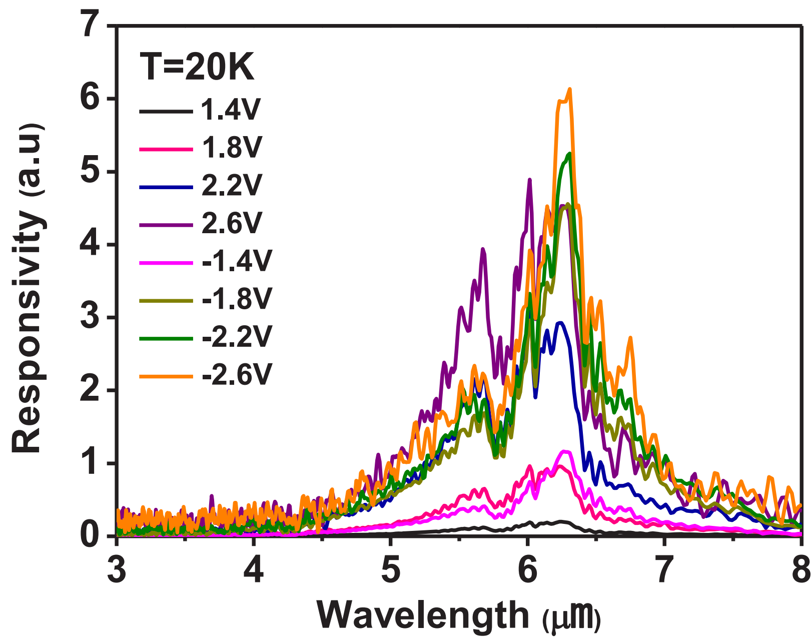

(a)

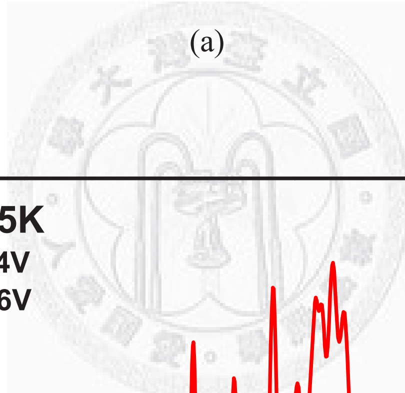

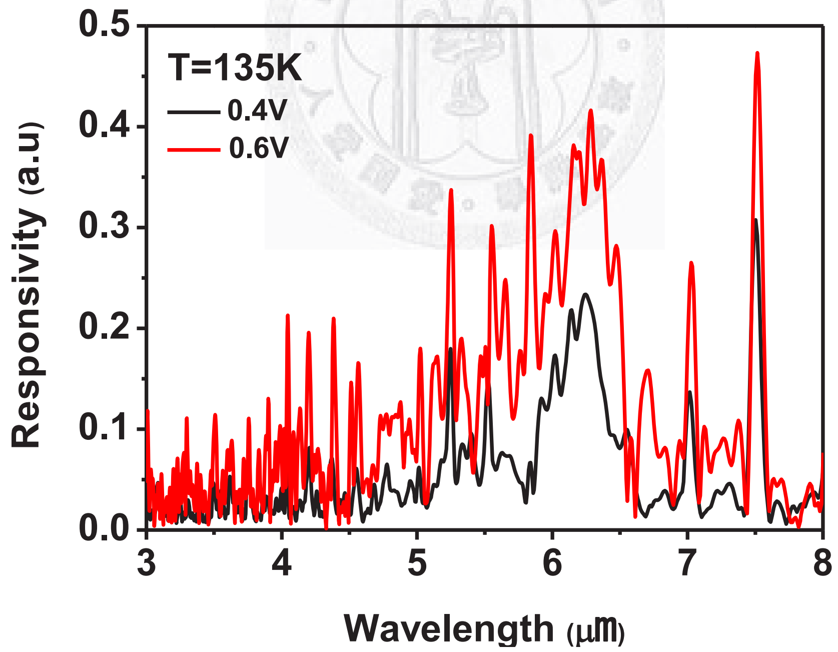

(b)

Fig. 4.13 The responsivities of device F at T= (a) 20 K and (b) 135 K (the highest operation temperature) at different biases.

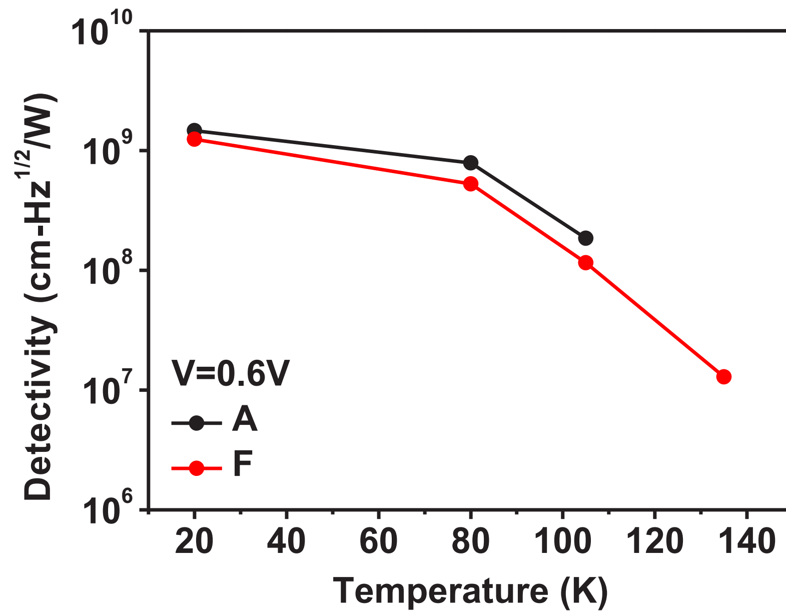

(a)

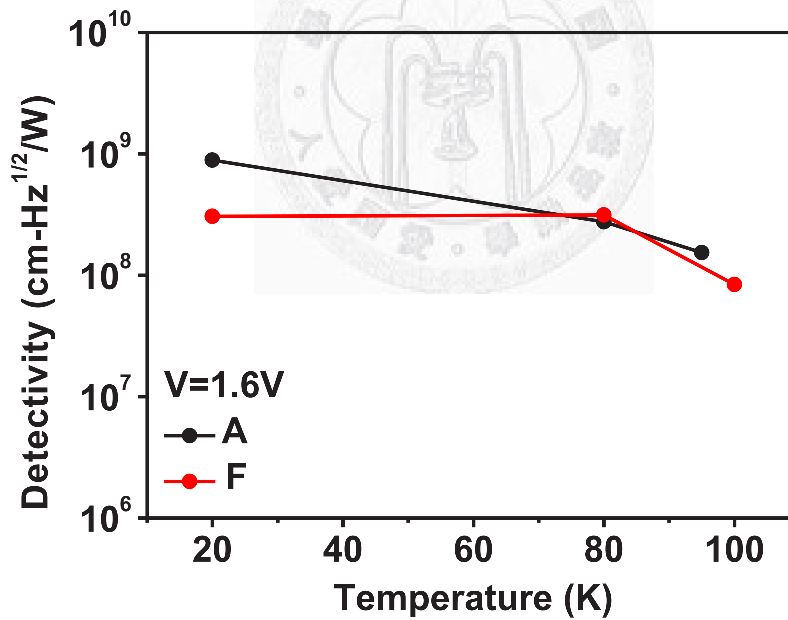

(b)

Fig. 4.14 The comparison of detectivities of devices A and F at bias voltage = (a) 0.6 volt and (b) 1.6 volt.

Chapter 5 Conclusions

The QDIPs with edge thinning structure and combination of edge thinning structure and surface passivation layer is investigated in this thesis respectively.

In chapter 3, the edge thinning structure with different depths on QDIPs is investigated. The edge thinning structure with width of 10 μm and thickness of 100~200 nm is adopted on n-i-n InAs/GaAs QDIPs at top contact layer and quantum dot layer respectively. It is found that edge thinning structure doesn't successfully reduce the dark current and enhance the operation temperature of QDIPs in this experiment.

In chapter 4, the combination of edge thinning structure with different depths and surface passivaiton layer Al_2O_3 with thickness of 10 nm is investigated. The combination of edge thinning structure and surface passivation layer Al_2O_3 doesn't successfully enhance the operation temperature of QDIPs in this experiment. However, the combination of edge thinning structure at quantum dot layer and surface passsivation layer Al_2O_3 can reduce the current so that the device can work at higher bias voltage.

In this thesis, edge thinning structure and the edge thinning structure combined with surface passivation layer Al_2O_3 don't enhance the operation temperature of QDIPs significantly. It may requires more advanced investigation.

Bibliography

[1] S. Raghavan, P. Rotella, A. Stintz, B. Fuchs, S. Krishna, C. Morath, D. A. Cardimona, and S. W. Kennerly, Appl. Phys. Lett. **81**,1369 (2002).

[2] H. Kaplan, Photonics Spectra, June, p.104 (1999).

[3] K. K. Choi, The Physics of Quantum Well Infrared Photodetectors, World Scientific, River Edge, New Jersey, (1997).

[4] A. G. U. Perera, W. Z. Shen, S. G. Matsik, H. C. Liu, M. Buchanan, and W. J. Schaff , Appl. Phys. Lett. **72**, 1596 (1998).

[5] Amlan Majumdar, K. K. Choi, J. L. Reno, and D. C. Tsui, Appl. Phys. Lett. **83**, 5130 (2003).

[6] M. Z. Tidrow, Xudong Jiang, Sheng S. Li, and K. Bacher, Appl. Phys. Lett. **74**, 1335 (1999).

[7] M. Z. Tidrow, J. C. Chiang, S. S. Li, and K. Bacher, Appl. Phys. Lett. **70**, 859 (1997).

[8] Amlan Majumdar, K. K. Choi, J. L. Reno, L. P. Rokhinson, and D. C. Tsui, Appl. Phys. Lett. **82**, 686 (2003).

[9] Adrienne D. Stiff-Roberts, Journal of Nanophotonics, **3**, 031607 (2009).

[10] S. Y. Wang, S. D. Lin, H. W. Wu, and C. P. Lee, Appl. Phys. Lett. **78**, 8 (2001).

[11] S. F. Tang, S. Y. Lin, and S. C. Lee, Appl. Phys. Lett. **78**, 17 (2001).

[12] P.Y. Lai, and S. C. Lee, “Passivation of Quantum Dot Infrared Photodetector with Al2O3 Deposited by Atomic Layer Deposition”, Graduate Institute of Electronics Engineering College of Electrical Engineering & Computer Science, National Taiwan University, Master Thesis.

[13] H. H. Lin, and S. C. Lee, Appl. Phys. Lett. **47** (8) (1985).

[14] Y. H. Wu, J. S. Su, W. C. Hsu, W. Lin, W. C. Liu, M. J. Kao, and R. T. Hsu, Jpn. J. Appl. Phys. **Vol. 34** (1995) pp. 5908-5911.

[15] S. Fu, T. P. Chen, R. C. Liu, S. Y. Cheng, P. H. Lai, Y. Y. Tsai, C. W. Hung, and W. C. Liu, Journal of The Electrochemical Society, **154** (4) H289-H292 (2007).

[16] Igor S. Altman , Physics Letters A 256(1999).122–124.

[17] Y. H. Wang, Jung-chi Chiang, and Sheng S. Li, J. Appl. Phys. 76 (4), 15 August (1994).

[18] Kim, MD; Noh, SK; Hong, SC, Appl. Phys. Lett. **82,553-555** (**2003)**.

[19] **M.O. Manasreh,** Semiconductor quantum wells **and superlattices for long-wavelength infrared detectors,** Boston : Artech House, c1993

[20] Amlan Majumdar, K. K. Choi, J. L. Reno ,Appl. Phys. Lett. **86**, 261110 (2005)

[21] G. Ariyawansa, A. G. U. Perera, G. Huang, and P. Bhattacharya, Appl. Phys. Lett. **94**, 131109 (2009)

[22] Y. H. Wang, Sheng S. Li, and Pin Ho, Appl. Phys. Lett. **62**, 93 (1993);

[23] P. Bhattacharya,a! X. H. Su, and S. Chakrabarti, Appl. Phys. Lett.**86**, 191106 (2005)

[24] J. Phillips, K. Kamath, and P. Bhattacharya, Appl. Phys. Lett. 72, 2020 (1998).

[25] S. Maimon, E. Finkman, and G. Bahir, Appl. Phys. Lett. 73, 2003 (1998).

[26] D. Pan, E. Towe, and S. Kennerly, Appl. Phys. Lett. 73, 1937 (1998).

[27] J. M. García, J. P. Silveira, and F. Briones, Appl. Phys. Lett. 77, 409 (2000).

[28] F. Guffarth, R. Heitz, A. Schliwa, O. Stier, N. N. Ledentsov, A. R. Kovsh, V. M. **Ustinov**, and D. Bimberg, Phys. Rev. B, **64**, 085305 (2001).

[29] P. B. Joyce, E. C. Le Ru, T. J. Krzyzewki, G. R. Bell, R. Murray, and T. S. Jones, Phys. Rev. B, **66**, 075316 (2002).

[30] K. Brunner, U. Bockelmann, G. Abstreiter, M. Walther, G. Böhm, G. Tränkle, and G. Weimann, J. Phys. (Paris) Colloq. **C5-3**, 107 (1993).

[31] T. Fukui, S. Ando, Y. Kokura, and T. Toriyama, Appl. Phys. Lett. **58**, 2018 (1991).

[32] Y. Nagamune, S. Tsukamoto, M. Nishioka, and Y. Arakawa, Appl. Phys. Lett. **64**, 2495 (1994).

[33] M. Grundmann, J. Christen, N. N. Ledentsov, J. Böhrer, D.Bimberg, S.S.Ruvimov, P. Werner, U. Richter, U. Gösele, J. Heydenreich, V. M. Ustinov, A. Yu.Egorov, P. S. Kop’ev, and Zh. I. Alferov, Phys. Rev. Lett. **74**, 4043

(1995).

[34] P.M. Petroff and S.P.DenBaars , Superlattices and Microstructures. 15,1(1994).

[35] D. Bimberg, M. Grundmann, and N. N. Ledentsov, Quantum Dot Heterostructures (J. Wiley & Sons, Chichester, 1999).

[36] Gallium Arsenide Materials, Devices, and Circuits, edited by M. J. Howes and D.V. Morgan (1985).

[37] Handbook of Instrumental Techniques for Analytical Chemistry, Ch.15, edited by C. P. Sherman Hsu.

[38] L. Goldstein, F. Glas, J. Y. Marzin, M. N. Charasse, and G. Le Roux, Appl. Phys. Lett. **47**, 1099 (1985).

[39] S. Z. Chang, T. C. Chang, and S. C. Lee, Appl. Surf. Sci. **92**, 70 (1996).

[40] Shiang-Feng Tang, Shih-Yen Lin, and Si-Chen Lee, Appl. Phys. Lett. **78**, 2428 (2001).

[41] Shih-Yen Lin, Yau-Ren Tsai, and Si-Chen Lee, Appl. Phys. Lett. **78**, 2784 (2001).

[42] J. D. Phillips, J. Appl. Phys. **91**, 4590 (2002).

[43] F. Y. Chang, C. C. Wu, and H. H. Lin, Appl. Phys. Lett. **82**, 4477 (2003).

[44] H. Petterson, L. Baath, N. Carlsson, W. Seifert, and L. Samuelson, Appl. Phys. Lett. **79**, 78 (2001).

[45] Shih-Yen Lin, Yau-Ren Tsai, and Si-Chen Lee, Appl. Phys. Lett. **83**, 752 (2003).

[46] Z. Ye, J. C. Campbell, Z. Chen, E. T. Kim, and A. Madhukar, J. Appl. Phys. **92**, 7462 (2002).

[47] S. Chakrabarti, A. D. Stiff-Roberts, P. Bhattacharya, S. Gunapala, S. Bandara, S. B. Rafol, and S. W. Kennerly, IEEE Photonics Technol. Lett. **16**, 1361 (2004).

[48] M. L. Huang, Y. C. Chang, C. H. Chang, Y. J. Lee, P. Chang, J. Kwo, T. B. Wu and M. Hong, "Surface passivation of III-V compound semiconductors using atomic-layer-deposition-grown Al_2O_3.", Appl. Phys. Letts. 87 252104 (2005).